Deep-Sea Research I 109 (2016) 10–26

Contents lists available at ScienceDirect

Deep-Sea Research I

journal homepage: www.elsevier.com/locate/dsri

Stirring by deep cyclones and the evolution of Denmark strait overflow water observed at line W

M. Andres [a,*], J.M. Toole [a], D.J. Torres [a], W.M. Smethie Jr. [b], T.M. Joyce [a], R.G. Curry [a]

[a] Woods Hole Oceanographic Institution, Woods Hole, MA 02543, USA
[b] Lamont-Doherty Earth Observatory, Palisades, NY 10964-8000, USA

ARTICLE INFO

Article history:
Received 20 August 2015
Received in revised form
25 November 2015
Accepted 24 December 2015
Available online 8 January 2016

ABSTRACT

Shipboard velocity and water property data from 18 transects across the North Atlantic Deep Western Boundary Current (DWBC) near 40 °N are examined to study the evolution of the Denmark Strait Overflow Water (DSOW) component of the DWBC and mixing between DSOW and the interior. The examined transects along Line W – which stretches from the continental shelf south of New England to Bermuda – were made between 1994 and 2014. The shipboard data comprise measurements at regular stations of velocity from lowered acoustic Doppler current profilers, CTD profiles and trace gas chlorofluorocarbon (CFC) concentrations from bottle samples at discrete depths. Comparison of the Line W velocity sections with concurrent sea surface height maps from satellite altimetry indicates that large cyclones in the deep ocean accompany intermittent quasi-stationary meander troughs in the Gulf Stream path at Line W. A composite of 5 velocity sections along Line W suggests that a typical cyclone reaches swirl speeds of greater than 30 cm s^{-1} at 3400-m depth and has a radius (distance between the center and the maximum velocity) of 75 km. Tracer data suggest that these cyclones affect not only the deep velocity structure along Line W, but also provide a mechanism for water exchange between the DWBC's DSOW and the interior. Vigorous exchange is corroborated by a mismatch in the CFC-11:CFC-12 and CFC-113:CFC-12 ratio ages calculated for DSOW at Line W. During the most recent 5-year period (2010–2014), a decrease in DSOW density has been driven by warming (increasing by almost 0.1 °C) as salinity has increased only slightly (by 0.003, which is close to the 0.002 uncertainty of the measurements). The abyssal ocean offshore of the DWBC and Gulf Stream and deeper than 3000-m depth has freshened at a rate of 6×10^{-4} yr^{-1} since at least 2003. Density here remains nearly unchanged over this period, due to temperature compensation, though a linear cooling trend in the abyssal ocean (to compensate the freshening) is not statistically significant.

1. Introduction

The North Atlantic's intermediate and deep waters are formed at high-latitudes via deep convection in the Labrador and Irminger Seas and from overflows of dense Nordic Seas waters over the Greenland–Iceland–Scotland Ridge (e.g., Swift, 1994; Pickart et al., 1997; Schott and Brandt, 2007). From their high-latitude formation regions, these dense waters – which comprise the cold limb of the Atlantic Meridional Overturning Circulation (AMOC) – infiltrate the deep ocean and spread towards the subtropics (Worthington and Wright, 1970; Talley and McCartney, 1982; Smethie et al., 2000; LeBel et al., 2008). Along the continental slope, the Deep Western Boundary Current (DWBC) rapidly transports equatorward part of the AMOC's cold limb flow (e.g., Watts, 1991; Bower and Hunt, 2000; Rhein et al., 2015). At 40 °N the DWBC's equatorward transport is 25.1 Sv with ±12.5 Sv standard deviation (Toole et al., 2011, reported for a fixed neutral density range: $27.800 \le \gamma \le 28.125$ kg m^{-3}, see also Johns et al. 1995 for previous estimates of DWBC transport near 68 °W). At 26.5 °N the DWBC transports 32 Sv with ±16 Sv standard deviation (Meinen et al., 2013, reported for a fixed depth range: 800–4800 dbar).

The importance of interior pathways for the AMOC's cold limb is suggested by tracer studies (Fine, 2011) and float experiments (Bower et al., 2009). The DWBC exchanges water with the interior ocean along its equatorward route (McCartney, 1992; Smethie et al., 2000; Fine et al., 2002). This exchange is likely enhanced in some regions, for example, where the DWBC rounds the Grand Banks near Newfoundland (Bower et al., 2013) and near Cape Hatteras where the poleward-flowing Gulf Stream crosses over the equatorward-flowing DWBC (Pickart and Smethie, 1993; Spall, 1996; Pickart, 1994). However, the relative importance of interior versus boundary current pathways and the temporal and spatial

* Corresponding author.
E-mail address: mandres@whoi.edu (M. Andres).

http://dx.doi.org/10.1016/j.dsr.2015.12.011
0967-0637/

variability of the processes that control exchange between the interior and the DWBC are not fully understood.

Since the early 1990s satellite altimetry has provided a near-global view of the surface ocean circulation. This surface view is complemented by Argo floats, which presently sample the oceans to 2000-m depth with more than 3000 floats globally to provide observations at about 3° horizontal spacing and 10-day sampling interval. Repeat expendable bathythermogaphs (XBTs) and acoustic Doppler current profilers (ADCPs) mounted on ships, provide additional information about the upper-ocean along repeat transects (Abraham et al., 2013; Rossby et al., 2014); this is particularly relevant across western boundary currents and on the continental slopes and shelves since these areas are generally not well resolved by Argo measurements. However, deep-ocean measurements are relatively sparse and much of the ocean below 2000 m remains under-sampled. In the absence of a basin-scale deep Argo program, in situ measurements such as those from deep moorings or repeated deep-reaching shipboard casts are required to develop a comprehensive view of the abyssal circulation's long-term average state and also to detect abyssal changes and evaluate whether the deep ocean is properly captured in numerical models.

Measurements along Line W have provided such deep in situ observations as one component of a long-term AMOC observational program in the North Atlantic. Line W stretches from the continental shelf south of New England towards Bermuda across the DWBC, which flows equatorward along the continental slope between the 2500-m and 4000-m isobaths (Joyce et al., 2005), and across the vigorously-meandering Gulf Stream downstream of its separation point by Cape Hatteras (Fig. 1). The sustained 10-year program along Line W – initiated in 2004 following previous field campaigns in the region and completed in spring 2014 – comprised moorings across the DWBC and repeated shipboard measurements collected once or twice per year at reoccupied stations between the 90-m isobath on the Middle Atlantic Bight shelf and the western flank of the Bermuda Rise.

Temporal variability of the DWBC at Line W between November 2001 and May 2008 has been reported based on temperature, salinity and velocity records from a mooring at "Station W" (at 39 °N, 69 °W) near the 3000-m isobath (Peña-Molino et al., 2011). The analysis, which emphasizes variability in the lightest constituents of the DWBC: upper- and deep-Labrador Sea Waters (uLSW and dLSW), shows that dLSW at Station W became about 0.2 °C warmer and saltier by 0.1 over that 6.5 year period while uLSW cooled and freshened. Furthermore, the depth of the potential vorticity minimum at Station W shoaled with time from about 1500-m depth to 700-m depth. These low frequency changes in the LSW properties may be linked to earlier changes in the central Labrador Sea (with lags between changes in the source region and changes in the DWBC at Line W ranging from 4 to 9 years, Peña-Molino et al., 2011).

Toole et al. (2011) report on the measurements from the five-element mooring array deployed for the first 4 years of the Line W program (2004–2008). Variability in the layer transports of uLSW, dLSW (or in their terminology, classical LSW, cLSW) and the

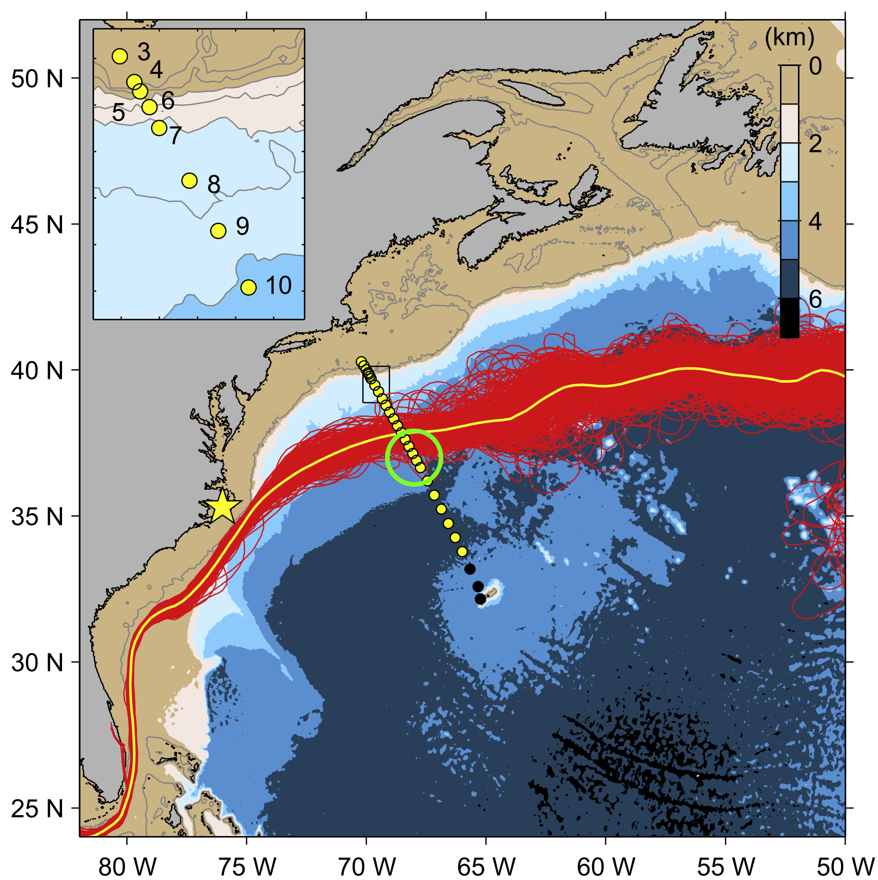

Fig. 1. Bathymetry of the western North Atlantic (shaded) showing Line W nominal station locations 1–26 (yellow dots) and the supplemental stations at the southeastern end sampled on some of the most recent cruises (stations 27–29, black dots). Stations 1–3 at the northwestern end of the line are on the Middle Atlantic Bight shelf. Black box indicates the area shown in the inset; inset shows isobaths at 200 m and from 500 m to 3000 m at 500-m increments (gray). The Gulf Stream meander envelope is indicated by the 40-cm contours (red) from monthly mean AVISO absolute dynamic topography maps with the mean of these paths also shown (yellow curve). Star indicates Cape Hatteras where the Gulf Stream detaches from the western boundary and a portion of the DWBC passes under the Gulf Stream. Green circle (37 °N, 68 °W) indicates the location of the SYNOP Central Array (Savidge and Bane, 1999a). Line W is named after L. Valentine Worthington who was a physical oceanographer at the Woods Hole Oceanographic Institution. (For interpretation of the references to color in this figure legend, the reader is referred to the web version of this article.)

Iceland–Scotland and Denmark Strait Overflow Waters (ISOW and DSOW) is striking. The mean (equatorward) transport summed over these four layers is 25.1 Sv, and the range is larger than the mean: transport varies from 3.5 Sv to 79.9 Sv (based on synoptic estimates every 5th-day). The area over the slope between the mean axis of the Gulf Stream and the Middle Atlantic Bight continental shelf break is an energetic region due to vigorous Gulf Stream meanders, pinched off warm core rings and topographic Rossby waves that propagate through the region (Cornillon, 1986; Gawarkiewicz et al., 2001; Thompson and Luyten, 1976). The former two are evident in the eddy kinetic energy derived from satellite altimetry (e.g., Kelly et al., 2010) and in the time-varying Gulf Stream path derived from the monthly mean maps of sea surface height (SSH) from satellite altimetry (Fig. 1, red curves). We hypothesize that much of the variability in the DWBC layer transports and velocities that is observed in the deep ocean with the Line W moorings is correlated with upper-ocean variability here, either due to a direct causal link between layers or due to independent responses of the layers to a common forcing.

The following discusses the shipboard data collected during the Line W program and several earlier field programs. Since previous research has focused on properties (Peña-Molino et al., 2011) and pathways (Bower et al., 2009) of the LSW component of the DWBC, the emphasis here is on the variability of DSOW, the densest component of the DWBC (aside from remnant Antarctic Bottom Water, AABW, which recirculates at Line W). DSOW contributes a significant fraction of the total overflow from the Nordic Seas into the North Atlantic (Våge et al., 2011; Jochumsen et al., 2012; van Aken and de Jong, 2012).

This paper serves to (1) characterize the upper- and deep ocean velocity structure and property distributions along Line W, (2) document the low frequency changes observed in DSOW at Line W and (3) examine the mechanisms by which upper- and deep ocean variability may be coupled here, resulting in exchange between the DWBC and the interior. Several auxiliary data sets are used to provide context for the variability observed with the shipboard measurements. Results from the final Line W mooring data will be reported elsewhere.

The shipboard and auxiliary data sets used in this study are introduced in Section 2. Section 3 describes the mean velocity structure derived from the LADCP data, explains the method used to identify the DSOW component of the DWBC and presents the time-varying characteristics of the DSOW and deep interior at Line W. Section 4 considers the shipboard observations in the context of historical measurements of deep cyclogenesis near Line W and resultant event-driven mixing between the DSOW and interior. Section 5 summarizes the findings of this study.

2. Data

2.1. Shipboard data

Line W shipboard observations include (1) full-depth temperature and salinity profiles processed to 2-dbar resolution made with CTDs, (2) horizontal velocity profiles from lowered ADCPs (LADCPs) generally processed to 10 or 20-dbar resolution, and (3) transient tracer concentrations from bottle samples taken at up to 23 or 24 discrete depths chosen to resolve the DWBC water property cores. Tracers include the chlorofluorocarbons: CCl_3F (CFC-11), CCl_2F_2 (CFC-12), and CCl_2FCClF_2 (CFC-13). I-129 concentrations were also measured at Line W and are reported on elsewhere (Smethie et al., 2012).

The water property and velocity measurements are from 26 fixed sites (or a subset of these) occupied once or twice per year from 2004 to 2014 (Fig. 1 and Table 1). Station spacing is most

Table 1
Physical Parameters for the Nominal Station Locations along Line W.

Station ID	No.[a]	Lat. (°N)	Lon. (°W)	Depth (m)	Distance[b] (km)	Spacing (km)	Rms[c] (km)	CS rms[d] (km)
1	3	40.29	70.21	90	−50.4		1.4	1.2
2	9	40.14	70.10	125	−32.2	18.2	0.9	0.8
3	12	40.01	70.01	164	−15.5	16.8	0.8	0.3
4	14	39.90	69.93	728	2.0	17.4	0.9	0.6
5	16	39.86	69.90	1154	4.1	2.1	1.8	1.1
6	14	39.79	69.85	1444	12.4	8.3	1.3	0.7
7	16	39.70	69.80	2079	23.2	10.8	4.6	0.9
8	14	39.48	69.64	2400	51.7	28.6	1.4	1.2
9	15	39.26	69.49	2635	79.0	27.3	7.0	0.8
10	15	39.02	69.33	3059	109.3	30.2	5.3	1.6
11	16	38.79	69.18	3253	137.4	28.1	3.7	1.8
12	16	38.56	69.03	3456	166.6	29.2	8.3	2.3
13	15	38.33	68.86	3814	195.8	29.2	2.9	1.8
14	15	38.09	68.70	4096	225.9	30.1	6.2	3.9
15	13	37.85	68.54	4363	256.0	30.1	5.9	5.4
16	16	37.62	68.38	4589	285.3	29.2	6.6	4.9
17	14	37.38	68.22	4746	315.4	30.1	4.0	3.4
18	12	37.14	68.06	4903	345.7	30.3	3.1	1.6
19	13	36.90	67.90	4933	376.0	30.4	3.5	2.3
20	10	36.66	67.74	4956	406.2	30.2	3.6	2.9
21	10	36.20	67.45	4989	463.2	57.0	2.4	1.9
22	8	35.71	67.16	5100	523.6	60.3	3.6	3.2
23	8	35.23	66.87	5093	583.4	59.8	2.7	1.8
24	7	34.74	66.58	5226	643.8	60.4	2.7	2.2
25	7	34.26	66.29	5212	703.4	59.6	1.8	1.2
26	7	33.78	66.00	5130	763.1	59.7	1.1	0.8
27	2	33.18	65.67	4203	836.9	73.9	8.9	5.5
28	2	32.58	65.33	4697	909.9	73.0	0.8	0.2
29	2	32.16	65.23	4099	956.5	46.5	0.3	0.2

[a] Number of cruises on which the station was sampled during the Line W program or an earlier cruise.
[b] Distance offshore of the 200 m isobath (39.8817 °N, 69.9361 °W).
[c] Root mean square difference between actual and nominal station locations.
[d] As in 3, but for the cross-stream direction, which is roughly perpendicular to the isobaths on the continental slope.

dense over the continental slope to resolve the DWBC there and ranges from a few km over the steepest part of the slope (spanning the 700-m to 1200-m isobaths, see the inset in Fig. 1) to 60-km spacing in the Sargasso Sea. Two of the most recent transects included additional stations (Stations 27–29) that extend the sampling to within 50 km of Bermuda.

The 15 Line W program transects include LADCP measurements at most stations (Table 2). Average property sections (including temperature and salinity) and LADCP-measured velocity sections from the first four years of the Line W program (2004–2008) are reported in Toole et al. (2011). Properties and velocities from eight sections taken prior to the Line W program have been reported previously (Joyce et al., 2005). While some of these earlier transects have relatively few stations in the DWBC and are excluded in the present analysis because they do not sample the DSOW, three (from 1994, 1995 and 2003) do sample the entire DWBC and include tracer data (Table 2). These are included here so the evolution of the DSOW over a longer period can be examined.

In total, concurrent LADCP and tracer data from 18 transects that crossed the DWBC between 1994 and 2014 are examined here. Of these, 8 sections reach to Station 26 in the Sargasso Sea (which is 760 km offshore of the Middle Atlantic Bight shelf break at the 200-m isobath), while 12 reach across the Gulf Stream to at least Station 20. The 2003 transect is an excerpt from a CLIVAR occupation of the A22 repeat section. The data, including those that predate the Line W program, are available through the Line W website (http://www.whoi.edu/science/PO/linew). Figures showing property sections and the cruise reports are also available through this website.

Table 2
Cruise Data for the Transects along Line W from the Line W Program (15) and Prior Programs (3).

Section #	Cruise ID	Month	Year	Stations Sampled[a]
1	EN257	Nov.	1994	5:7 9:14 16
2	OC269	Jun.	1995	5 7 9 11:14 16
3	KN173-2	Oct.	2003	3:26
4	OC401	May	2004	3:20
5	KZ1204	Sep.	2004	3:24 (25) 26
6	OC411	Apr.	2005	(1) 2:22
7	OC417	Oct.	2005	1 2 4:12 16:19
8	OC421	Apr.	2006	(1 2) 3:8 (9) 10:17
9	OC432	Oct.	2006	(1 2) 3:21
10	OC436	Apr.	2007	(2) 3:5 7:19
11	EN440	Oct.	2007	(1) 2:26
12	OC446	May	2008	(1) 2:8 (9) 10:17
13	EN466	Sep.	2009	(1:3) 4:17 (18:24) 25 26
14	AT17	Oct.	2010	1:17 19 21 23 25 26
15	OC472	Jul.	2011	1 2 (3) 4:25
16	KN208	Aug.	2012	(1) 2:29
17	EN525	May	2013	2:26
18	KN218	May	2014	2:29

[a] Only property data are available for the stations in parentheses.

2.1.1. CTD and LADCP data

Seabird 911plus conductivity–temperature–depth (CTD) instruments were mounted on a rosette frame to obtain full-water column hydrographic measurements of pressure, conductivity, and temperature. The CTD sensors were generally calibrated prior to or just after each cruise. The salinity (conductivity) data were further refined with bottle samples (Millard and Yang, 1993); salinity is reported as practical salinity throughout this paper. Uncertainties in the hydrographic measurements have been estimated as 1 dbar, 0.001 °C and 0.002 for salinity (Toole et al., 2011).

Velocity data were measured using a LADCP system that consisted of an upward-facing 300 kHz ADCP and a downward-facing 150 kHz ADCP from Teledyne, RD Instruments. A depth-dependent ADCP setup procedure was implemented. Stations with depths greater than 1500 m had the bottom-facing 150 kHz ADCP set to collect 16-m bins and the upward-facing 300 kHz ADCP set for 8-m bins. Shallower stations used 8-m and 4-m bin sizes, respectively. This was designed to maximize the ADCP range while minimizing single-ping standard deviations in the very low-scatter deep waters south of the Gulf Stream. Raw LADCP data were merged with CTD and navigation data and processed using the inverse method described in Visbeck (2002) and Thurnherr (2010). This method solves a set of linear equations defined by the LADCP velocity measurements (which are a sum of ocean and instrument platform velocities plus noise). Additional velocity profile referencing constraints can be added to the system of linear equations. Typical available constraints are derived from shipboard ADCP profiles near the surface, bottom track data near the bottom, and mean ship drift from GPS. Thurnherr (2010) found that using 2 or more additional constraints, reduced velocity errors to $\sim$3 cm/s rms when compared to independent mooring measurements. In all LADCP data presented here, all 3 constraints were applied to estimate absolute velocity profiles. We estimate LADCP absolute velocity errors to be $\sim$3 cm/s rms. Each resultant absolute velocity profile was de-tided by subtracting the barotropic tidal velocity as computed by a 1/12° resolution regional barotropic inverse tidal model developed at Oregon State University (http://volkov.oce.orst.edu/tides/region.html, see also Egbert et al., 1994; Egbert and Erofeeva, 2002). The magnitude of the barotropic tide was found to be <2 cm/s for stations with 900-m water depth or greater. For stations with less than 900-m depth, tidal magnitude was less than 5 cm/s. We expect additional error from the tidal model to be <1 cm/s for all stations. We estimate total LADCP absolute velocity errors at 3–4 cm/s.

2.1.2. Bottle data

Water samples were collected in 10-L Niskin bottles on a 24-bottle rosette. Frequently, one site on the rosette was occupied by the LADCP, limiting samples to at most 23 depths at each station on those cruises (except for the October 2003 CLIVAR cruise, which had a 36-bottle rosette). Water samples were analyzed onboard ship for salts and dissolved oxygen and for the tracer concentration measurements (CFCs). The reported precision of the tracer measurements is between 0.5% and 1% for CFC-11 and CFC-12 and between 1% and 2% for CFC-113. CFCs are reported using the SIO98 calibration scale. Further details are provided in the cruise reports available from the Line W website.

2.2. Altimetry

The region's sea surface height (SSH) field during each Line W section is examined here using maps of absolute dynamic topography (MADT) to help establish the position of the Gulf Stream at Line W and also to identify meanders and rings that cross the line. A subset of these maps is shown in Fig. 2; the full set of SSH maps concurrent with all 18 crossings is available on the Line W website. The ¼° resolution gridded MADT product is generated from all available satellite altimetry data and maps are available at daily increments (though the repeat cycle of the Jason-2 satellite is about 10 days). The mapped data are produced by Ssalto/Duacs and distributed by AVISO, with support from CNES (http://www.aviso.altimetry.fr/duacs/). Line W is situated along Jason-2 satellite track number 126 (formerly occupied by Jason-1 and TOPEX/Poseidon).

The SSH maps (Fig. 2 and the Line W website) represent a snapshot during or just before each cruise. These data have not been deseasoned, so the differences from one panel to the next may include a small steric contribution due to seasonal heating and cooling. However, within each panel, the SSH gradients identify the strong surface geostrophic currents associated with the Gulf Stream and rings. In each panel, the yellow-shaded band identifies the Gulf Stream axis (i.e., roughly the 40-cm SSH contour), which flows towards the east-northeast. The path is sometimes contorted due to meanders of the current. These meanders generally propagate downstream (eastward) through the region (Cornillon, 1986).

2.3. Atmospheric transients

The anthropogenic trace gasses CFC-11, CFC-12 and CFC-13 are relatively well mixed in the atmosphere and their time-varying atmospheric concentrations are known (e.g., Walker et al., 2000; Prinn et al., 2000). These gasses are soluble in seawater and can serve as tracers to identify water masses and – under certain conditions – may indicate when a water parcel was last in contact with the atmosphere to help constrain oceanic spreading rates (Smethie et al., 2000; Fine, 2011).

The atmospheric concentrations of these transients are available at http://cdiac.ornl.gov/oceans/new_atmCFC.html. Atmospheric CFC-11 and CFC-113 concentrations increased until the 1990s and CFC-12 concentration increased until the early 2000s (Fig. 3a). Presently, atmospheric CFC concentrations are all decreasing. Although the concentration of CFC-12 in the atmosphere is greater than that of CFC-11 (their ratio is shown in Fig. 3b), their concentrations in seawater depend on each gas's solubility, so CFC-11 is generally present at higher concentrations in seawater than is CFC-12 (Fig. 3c). While the absolute CFC concentrations in seawater depend on the solubility of each compound and the percent saturation when water parcels were last at the sea surface, the

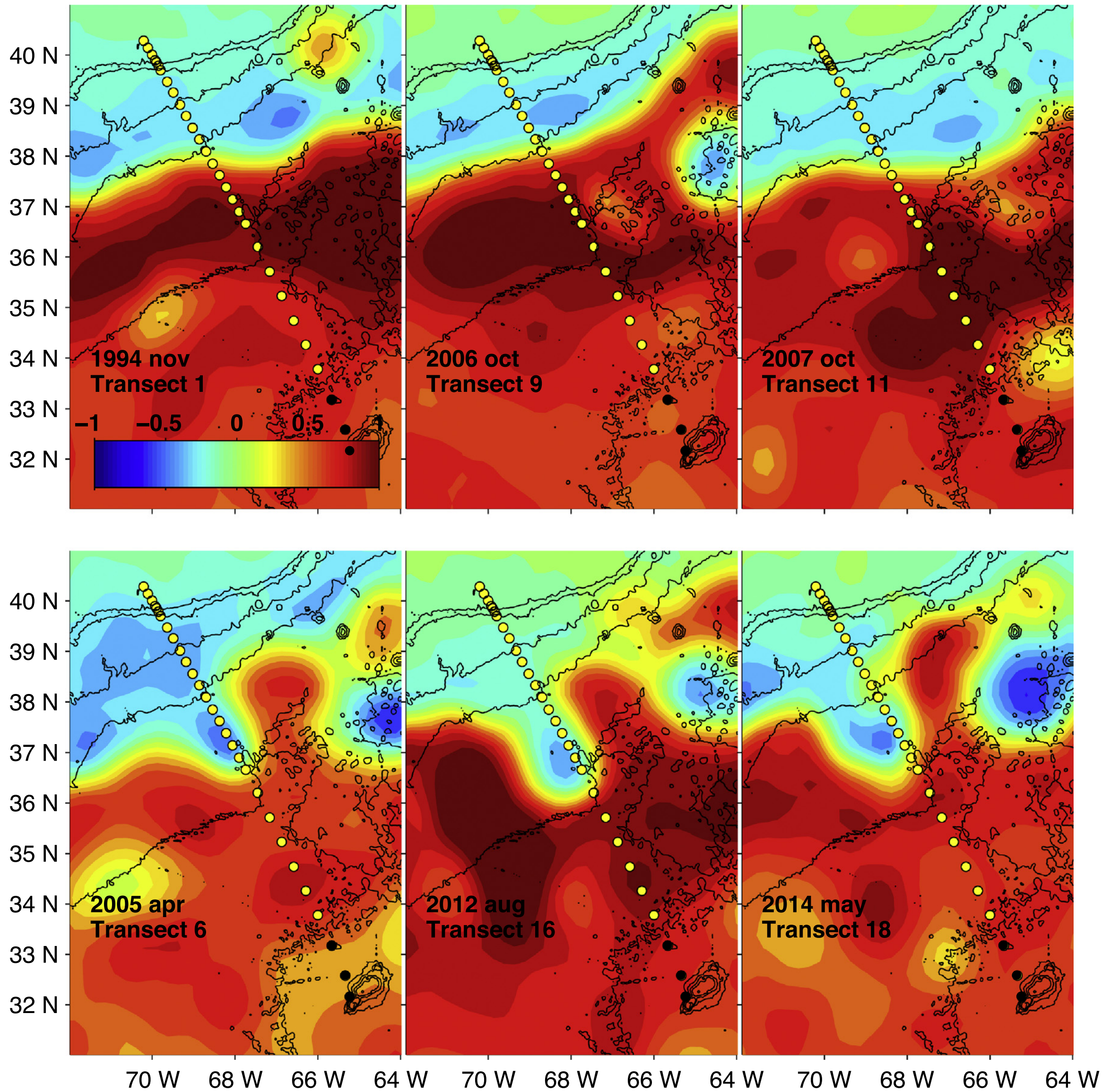

Fig. 2. Maps of SSH, shaded from −1 m (blue) to 1 m (red), during six of the Line W transects based on MADT from AVISO. Black contours show isobaths at 1000-m increments to a maximum of 5000-m depth. Dots indicate the nominal Line W station locations 1–26 (yellow) and the supplemental stations 27–29 (black). Upper row shows representative examples of a straight Gulf Stream path at Line W; bottom row shows examples of a Gulf Stream trough at Line W. For mapped SSH snapshots during each of the remaining 18 Line W transects, see the Line W website. (For interpretation of the references to color in this figure legend, the reader is referred to the web version of this article.)

CFC-11:CFC-12 ratio (or CFC-113:CFC-12 ratio) is independent of saturation (and only weakly dependent on temperature and salinity of the water parcel in contact with the atmosphere, Fig. 3c).

If a water parcel does not mix or mixes with water devoid of CFCs, its CFC ratio will be preserved (though as a consequence of such mixing, its CFC concentrations will decrease). In either of these two scenarios, CFC-11:CFC-12 (or CFC-113:CFC-12) measured in seawater can be compared with the time varying signature of atmospheric exposure (Fig. 3c) to estimate the time since the parcel was ventilated and to estimate, for example, the spreading rate of the DWBC waters (Pickart et al., 1989). It will be shown here that this assumption of no mixing with waters having older CFC signatures is likely not valid within the DSOW core. Rather, the mismatch between CFC-11:CFC-12 and CFC-113:CFC-12 derived ages found here is interpreted (Section 4.3.1) as evidence for significant exchange between DSOW and the interior. This exchange is corroborated by the increase over time in the CFC concentrations of the deep interior away from the western boundary (Section 4.4) and by the shape of the CFC concentration curves along a deep isopycnal in the Line W sections (Section 4.2).

3. Structure of the DWBC and gulf stream

3.1. Velocity sections and the gulf stream path

To examine the velocity structure along Line W and to compare the shipboard data with mooring data from Line W (Toole et al., 2011), LADCP-measured velocities from each transect are first rotated into the along-track (x) and cross-track (y) coordinates with y directed 61° east of North to obtain the along-track and cross-track velocities (u, v). Since variability in station locations is relatively small from one cruise to the next (less than 9 km root mean square difference for each station, Table 1), the rotated velocities are simply averaged by station to generate an Eulerian mean (Fig. 4a and b). This mean is calculated from varying numbers of samples at each station with relatively fewer data for the onshore-most (1–2) and offshore-most (27–29) sites. Nevertheless, the mean clearly shows the surface-intensified, poleward-flowing Gulf Stream and a comparatively weak equatorward flow beneath the

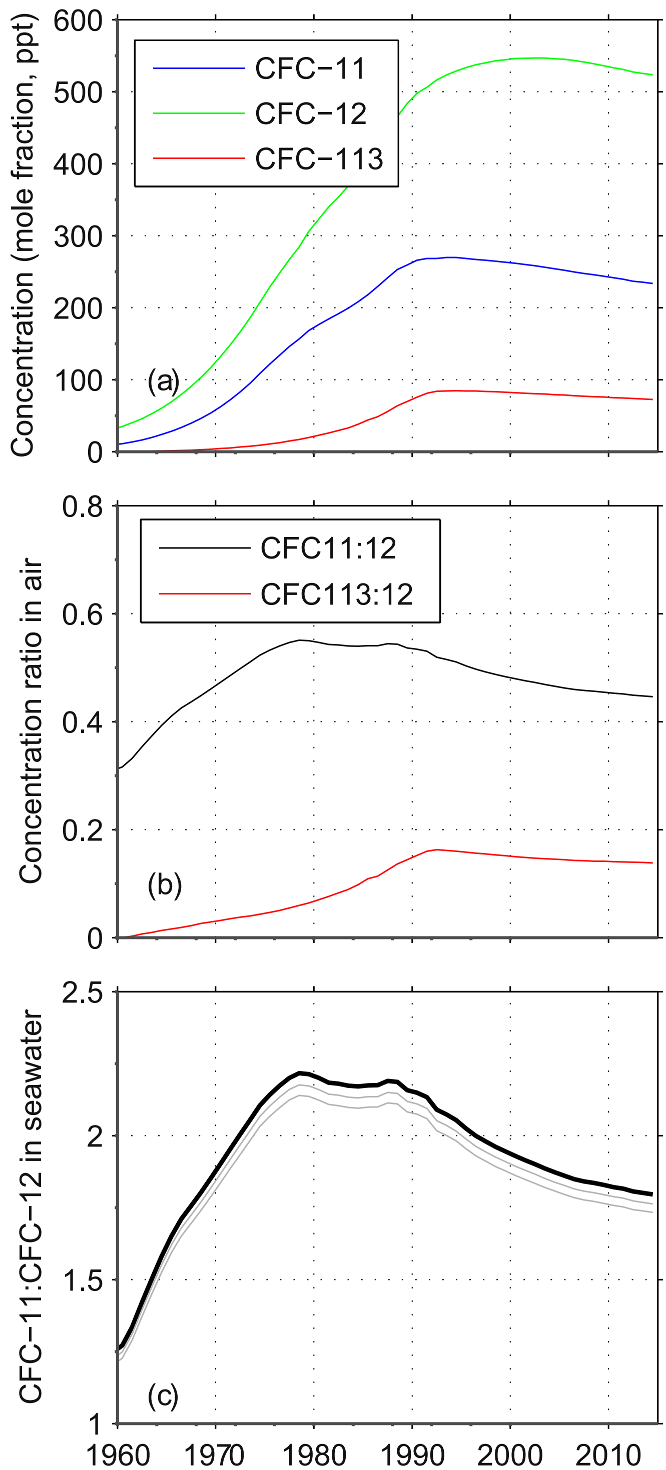

Fig. 3. Time evolution of northern hemisphere (a) atmospheric CFC concentrations and (b) atmospheric CFC ratios. Data are from Bullister (2015) and available at http://cdiac.ornl.gov/oceans/new_atmCFC.html and use the SIO98 calibration scale. Panel (c) shows the ratio of CFC-11 to CFC-12 in seawater calculated from the atmospheric concentrations and solubilities for seawater at 34.9 psu and 2.4 °C (black curve). Solubilities are temperature (and slightly salinity) dependent, with CFC-11 solubility more sensitive to temperature than CFC-12 (e.g., see Fig. 4 of Wallace, 1995); this slight difference in the temperature dependence is indicated by the CFC-11 to CFC-12 ratios for 34.9 psu and 5 °C and 7.5 °C (gray curves). (For interpretation of the references to color in this figure legend, the reader is referred to the web version of this article.)

Gulf Stream and over much of the slope. This equatorward flow has a local maximum near the bottom at the 3500-m to 4000-m isobaths.

Since this is not a stream-coordinates average, the Gulf Stream's strength is underestimated and its width overestimated due to the Stream's vigorous meandering as it crosses Line W. Furthermore, large offshore shifts of the Gulf Stream axis sampled during transects 6, 8, 15, 16 and 18 (see Fig. 2 bottom row and Line W website and also Table 2 for information about the transects) cause the ensemble mean to have a double velocity core that is not characteristic of the synoptic Gulf Stream structure.

A more representative depiction of the Gulf Stream velocity structure along Line W is generated by averaging only those sections that do not sample through a meander trough (Fig. 5, with the corresponding SSH composite shown in Fig. 6**b**). This eliminates the spurious double velocity core and shows the well documented "tilt" of the Gulf Stream (e.g., Johns et al., 1995; Richardson, 1985): the location of the maximum velocity at a given depth level is further offshore deeper in the water column (indicated with the gray dotted line in Fig. 5). This tilt is not confined to the upper ocean; weak (<10 cm s^{-1}), positive (poleward) velocities extend from the base of the thermocline to the seafloor about 150 km offshore of the upper-ocean Gulf Stream axis (i.e., between the gray arrows in Fig. 5).

In this mean velocity section (Fig. 5), a pronounced feature in the abyssal ocean is the region of negative (equatorward) cross-track velocity directly below the strongest surface-intensified Gulf Stream. This region reaches from about 1500-m depth to the seafloor and the mean cross-track velocity reaches -12 cm s^{-1} at 3400-m depth (centered on Station 15, about 250 km from the shelf break, see the yellow arrow in Fig. 5). While this flow is likely part of the DWBC, it is not where the highest CFC concentrations are found; the CFC concentration maxima are generally found closer to the boundary along the slope (see Section 3.2).

In addition to this equatorward flow directly beneath the Gulf Stream, part of the DWBC flows over the slope between the 2000-m and 4000-m isobaths. In particular, a velocity maximum in the density layer associated with the DSOW component of the DWBC is located near the bottom on the slope between the 3500-m and 4000-m isobaths, centered on Station 12, about 165 km offshore of the shelf break (blue arrow in Fig. 5). This deep structure is similar to that shown Fig. 4 for the full 18-section mean.

Both the 13- and 18-section means show weak (<2 cm s^{-1}) poleward flow directly over the bottom, upslope of the 3000-m isobath. This is roughly in the density layer of Iceland–Scotland Overflow Water (ISOW) and is in the opposite direction to what is expected for the DWBC and in contrast to the results from long-term mooring observations (e.g., see the Eulerian mean in Fig. 4 of Toole et al., 2011, which shows weak equatorward flow here). However, the magnitude of the LADCP-derived mean here (<2 cm s^{-1}) is smaller than the mean standard error of the flow, so this area of positive flow is not statistically different than no flow (or weakly negative, i.e., equatorward, flow).

In contrast to the mean generated from the LADCP sections that cross through a straight Gulf Stream path, the mean v and u for the 5 sections that sample through a meander trough has a less "tilted" Gulf Stream between the surface and 1000-m depth and the upper-layer's surface-intensified flow is aligned with the deep-reaching sub-thermocline poleward flow, which reaches 18 cm s^{-1} between 3500-m and 4000-m depth (Fig. 7, red arrow, with the corresponding SSH composite shown in Fig. 6a). Additionally, the equatorward flow (that was beneath the Gulf Stream in Fig. 5) is more pronounced (reaching -22 cm s^{-1}) and stretches from the near-surface to the seafloor, centered on Station 17 (Fig. 7, blue arrow). Comparison with observations from previous in situ measurements in the region suggests that this equatorward flow –

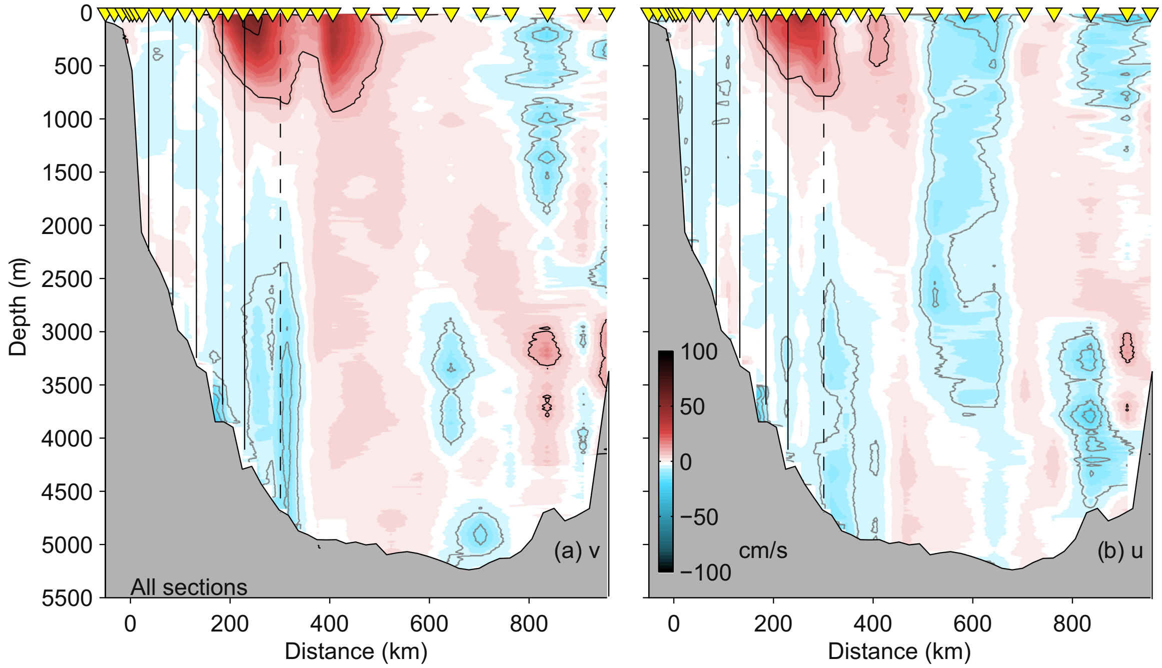

Fig. 4. Eulerian mean of velocity in the (a) v (cross-track) and (b) u (along-track) directions (rotated 61° east of North) from all 18 available LADCP sections. Gray contours highlight the structure of the negative velocities (and are at -5 cm s^{-1}, -10 cm s^{-1} and -15 cm s^{-1}); black contours are at 10 cm s^{-1} and 50 cm s^{-1}. Vertical lines indicate locations of Line W moorings (numbered 1 through 6 from left to right), with dashed line indicating mooring 6 (deployed only in the more recent settings of the Line W array). Yellow triangles indicate nominal Line W station locations. (For interpretation of the references to color in this figure legend, the reader is referred to the web version of this article.)

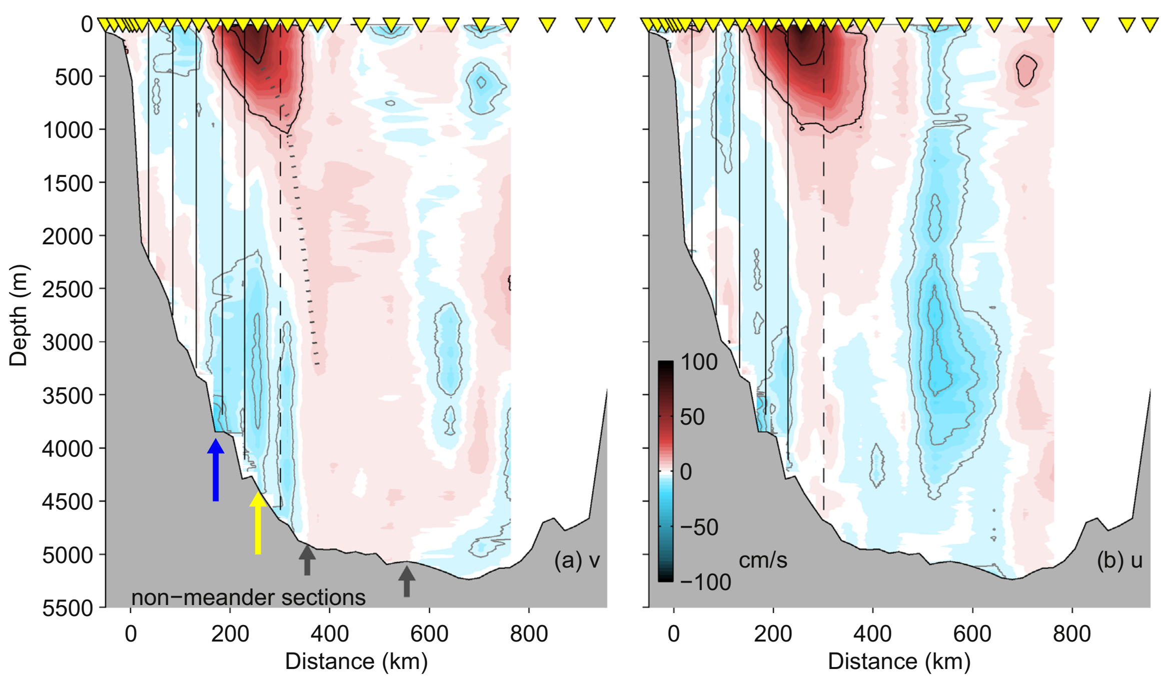

Fig. 5. Eulerian mean of (a) v and (b) u for the 13 sections that do not sample through a Gulf Stream meander trough. Yellow arrow highlights the core of equatorward flow aligned beneath the Gulf Stream and blue arrow highlights the velocity maximum associated with DSOW. Gray dotted line highlights the "tilt" in the Gulf Stream; dark gray arrows highlight the edges of the deep poleward velocities offset from the upper ocean Gulf Stream flow. Vertical lines, symbols and contours as in Fig. 4. (For interpretation of the references to color in this figure legend, the reader is referred to the web version of this article.)

together with the barotropic component of the above-mentioned poleward flow superimposed on the Gulf Stream – forms a deep cyclonic circulation. This interpretation of the flow is discussed further in Section 4.1.

In each section occupation, it is possible to identify a deep CFC maximum over the continental slope in the density range expected for DSOW, but often the corresponding LADCP section does not show a co-located maximum in the equatorward velocity. Though the mean sections (Figs. 4 and 5) clearly indicate a bottom-intensified velocity core on the slope near the depth expected for the DSOW (blue arrow in Fig. 5a), Gulf Stream meanders seem to disrupt this equatorward flow here (Fig. 7). Topographic Rossby

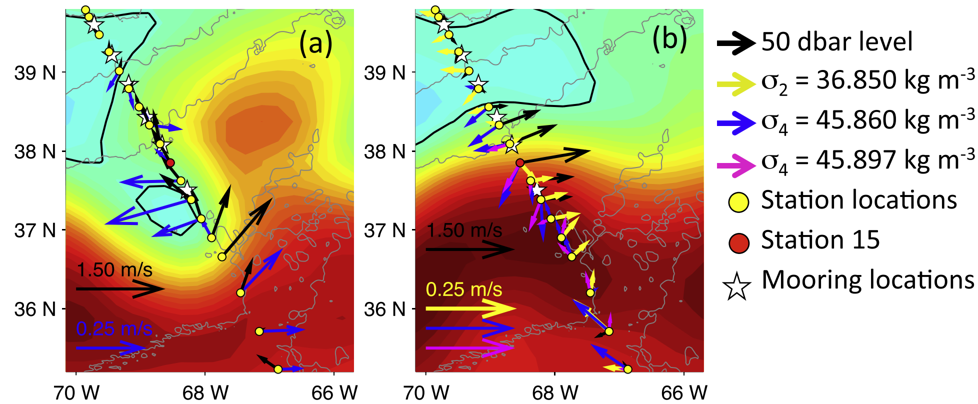

Fig. 6. Composite SSH maps (shaded). Panel (a) is the composite during the five sections when Gulf Stream path at Line W was in a large meander trough (Section 6, 8, 15, 16 and 18). Panel (b) is the composite for the 13 sections during non-meander paths of the Gulf Stream. For each case, the velocity vectors averaged over the corresponding LADCP sections are shown for the flow at the levels indicated in the legend. For clarity, yellow and magenta vectors are not included in panel (a). Colorbar and symbols as in Fig. 2, with Station 15 highlighted in red. The 17-cm SSH contour, which is closed north of the trough in panel (a), is highlighted in black. Line W mooring locations (white stars) are numbered 1–6 from northwest to southeast. (For interpretation of the references to color in this figure legend, the reader is referred to the web version of this article.)

waves, possibly forced by Gulf Stream meanders, are ubiquitous on the slope (e.g., Thompson and Luyten, 1976; Hogg, 2000; Pickart, 1995) and can obscure the mean (equatorward) DSOW flow in an individual velocity transect.

3.2. DSOW from maxima in transient tracer concentrations

In general, the sections along Line W have elevated CFC-11 concentrations in the surface waters and a pronounced minimum at the depth of the main thermocline (e.g., Fig. 8a and b). Concentrations are also elevated at the depths and densities of LSW with concentrations highest on or near the western boundary and decreasing into the Sargasso Sea. In the abyssal ocean (> 3000-m depth) there is a local CFC concentration maximum on the western boundary at the density expected for DSOW. Concentrations in the deep interior are low, though here, as in the rest of the Line W transect, concentrations do increase over time from one section to the next as a result of the changing atmospheric CFC concentrations and mixing of the more recently ventilated waters with the interior.

The CFC concentration maxima in the deep waters over the slope are used here to help identify the DSOW component of the DWBC and to investigate temporal variability in this water mass. Further, ratios of CFCs are used to produce spreading rate estimates, though since these estimates depend on the assumption that the DSOW in the DWBC is not mixing or is only mixing with an end member that is essentially free of CFCs, the estimates are likely biased.

For each Line W transect, the CFC bottle data are first evaluated to identify and smooth individual bottle samples below 2750 dbar that have anomalously high CFC concentration relative to their immediate vertical and horizontal neighbors. These could reflect very localized, small-scale oceanic inhomogeneities or a bottle that did not close completely. Of 1814 bottle samples taken at pressures

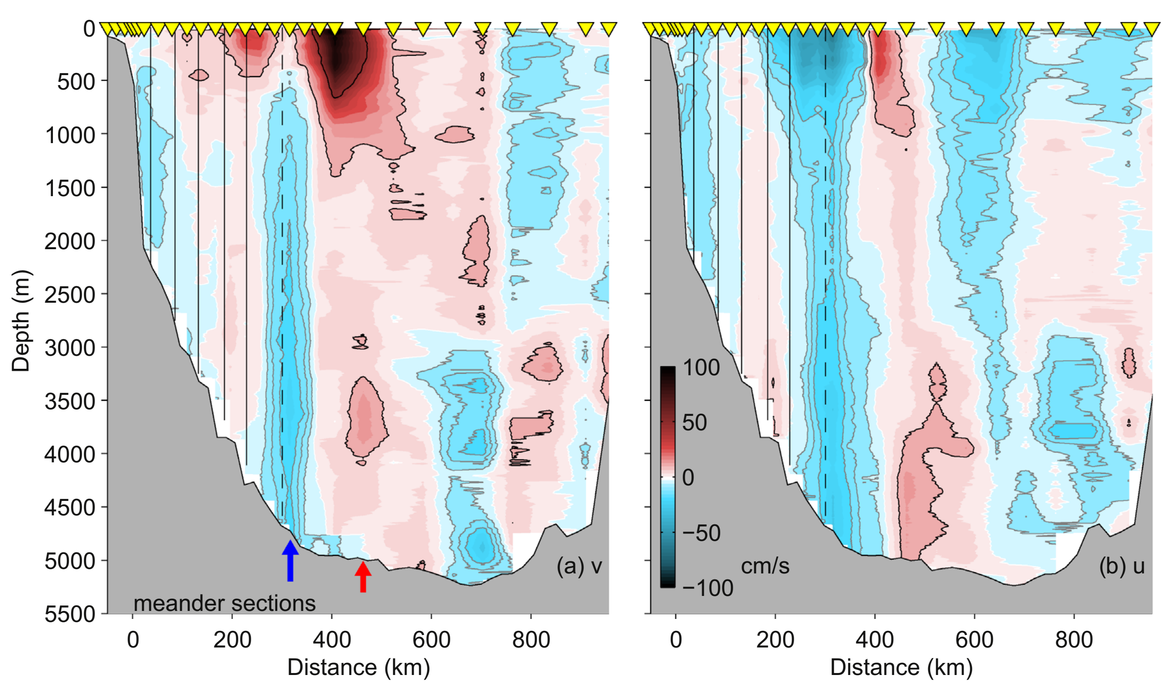

Fig. 7. Eulerian mean of (a) v and (b) u for 5 Section (6, 8, 15, 16, and 18) that sampled a Gulf Stream meander trough. Red and blue arrows highlight flow features discussed in the text. Vertical lines, symbols and contours as in Fig. 4. (For interpretation of the references to color in this figure legend, the reader is referred to the web version of this article.)

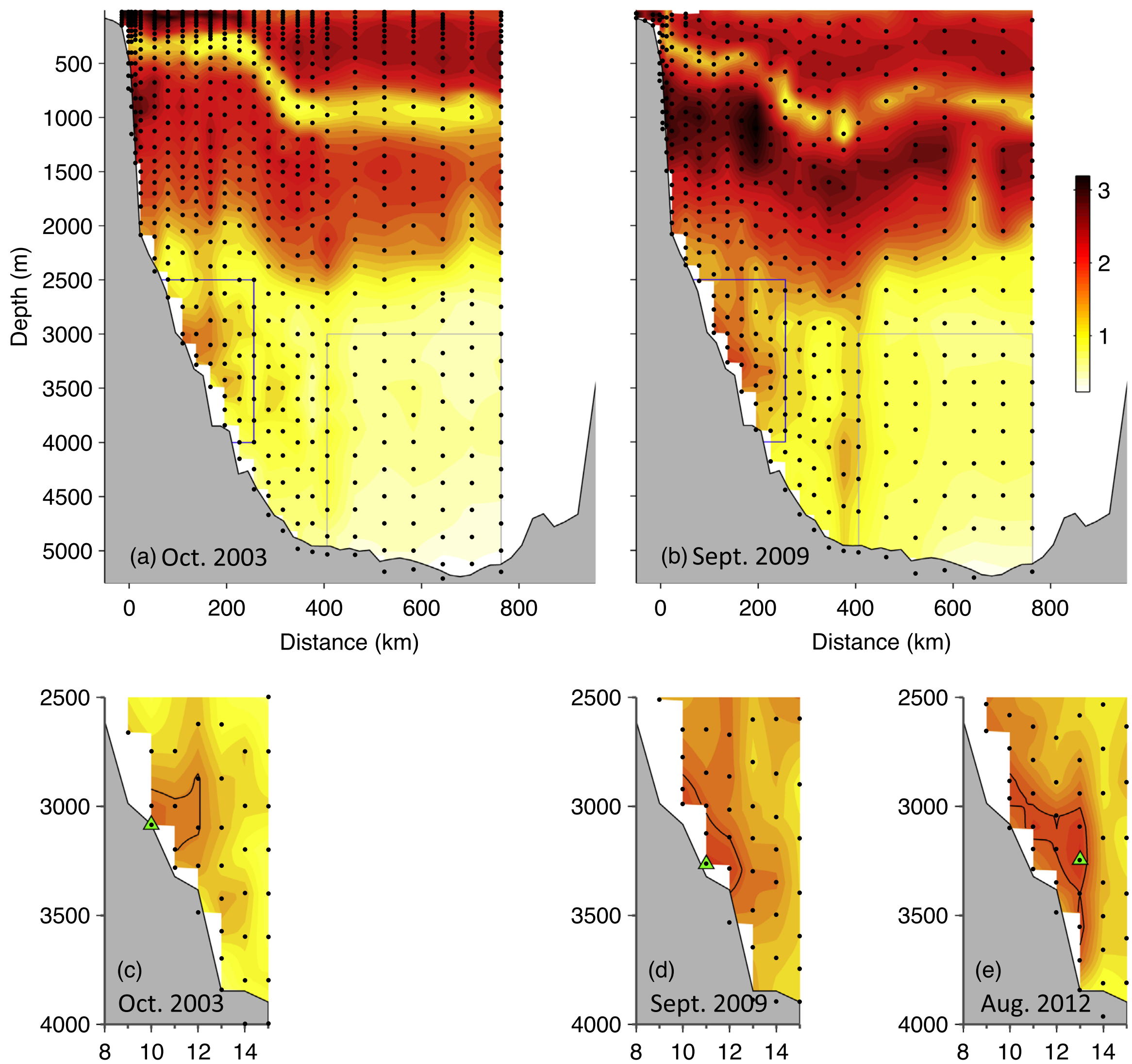

Fig. 8. CFC-11 concentrations (pmol kg^{-1}) along Line W for (a) October 2003 and (b) September 2009. Close ups of the regions denoted by the blue boxes are shown in (c) and (d), respectively, to highlight the DSOW. Station numbers are indicated on the *x*-axis. Locations of bottle samples (dots), local CFC-11 maximum in each section (green triangle) and region with CFC-11 concentration $\geq 90\%$ of the maximum value (black contour) are indicated. Panel (e) shows a close up of the DSOW for August 2012, when the Gulf Stream at Line W was in a large offshore meander (Fig. 2, transect 16). Gray boxes in (a) and (b) indicate the region over which the deep interior CFC concentrations are calculated for each section (see text). (For interpretation of the references to color in this figure legend, the reader is referred to the web version of this article.)

of 2750 dbar or greater, three ($<0.2\%$) are smoothed by linear interpolation between the neighboring sites. For each of these three, the percent difference in CFC-11 concentrations between the sample and its vertical neighbors (up or down the cast) is greater than 20%. After this minimal smoothing, the bottle data from each cast are linearly interpolated onto a 5-dbar vertical grid. The continuous CTD data are decimated onto the same grid. In the following, the gridded data are used to identify the CFC maxima associated with DSOW, delineate the DSOW core in each section, and find CFC concentrations on a deep isopycnal.

The position (vertical bin and station location) of the CFC-11 maximum below 2750 dbar (e.g., Fig. 8c–e, green triangles) is identified to help locate the DSOW water mass in each section. For most sections, the locations of the CFC-11 and CFC-12 maxima coincide. Since CFC-113 concentrations in the DWBC are low, particularly in the earliest sections, CFC-113 concentration is generally not used here to identify the DSOW except in sections 8 and 15, in which the CFC-11 and CFC-12 maxima do not coincide. For these two sections, the CFC-113 maximum is used to locate the DSOW water mass (in both cases, this CFC-113 maximum still falls within the general region of elevated CFC-11 and CFC-12 concentrations). The horizontal position of the DSOW CFC maximum varies over 86 km (Stations 10–13) and its depth ranges by almost 700 m, with deeper cores generally occurring further offshore.

3.3. Properties in the DSOW core and the deep interior

With these DSOW maximum CFC concentrations and locations established (Fig. 9), the "core" of DSOW present in each section is identified in a manner similar to the methodology of Pickart and Smethie (1998). The locations (in the gridded data) deeper than 2850 dbar with CFC-11 concentrations within 90% of the deep maximum CFC-11 concentration are classified here as the DSOW core. The gridded CFC concentrations, salinities and potential temperatures referenced to 0 dbar (θ_0) within this patch are averaged for each section to quantify the time evolution of the core DSOW properties at Line W (Fig. 10 b–d). The potential temperatures and salinities of the DSOW core (identified using the CFC distributions) fall within the range reported for typical DSOW (1–2.5 °C and 34.86–34.90 salinity, van Aken and de Jong, 2012).

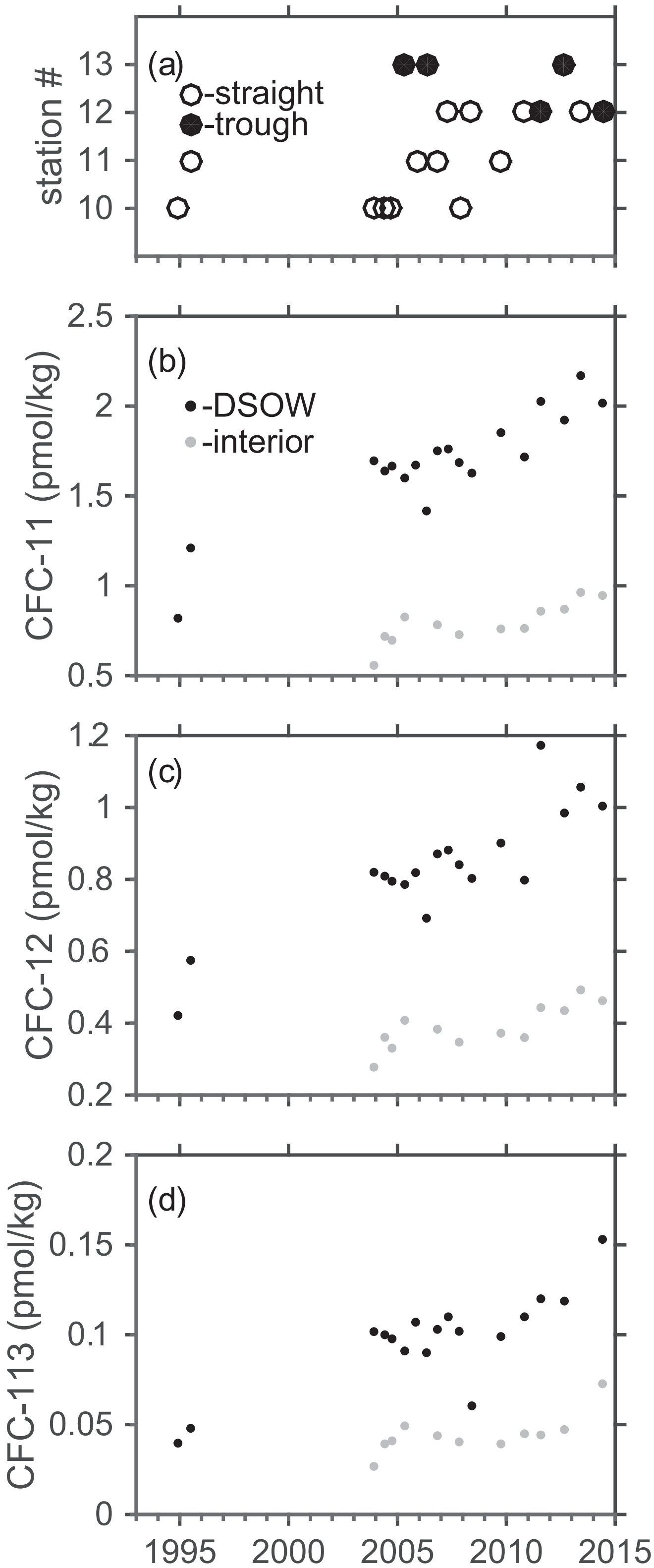

Fig. 9. Time series showing the evolving characteristics at Line W of DSOW and the deep interior for each occupation (with the latter averaged over the area in the gray box shown in Fig. 8). Panel (a) shows the location of the DSOW, reported as the station where the deep maximum CFC concentration is observed (see text); filled symbols highlight the occupations when the upper ocean Gulf Stream was in a large meander at Line W. Concentrations at the (single-point) maximum CFC location (black) and averaged across the deep interior (gray) are shown for: (b) CFC-11, (c) CFC-12, and (d) CFC-113 (there are no CFC-113 concentration data available for May 2013, transect 17).

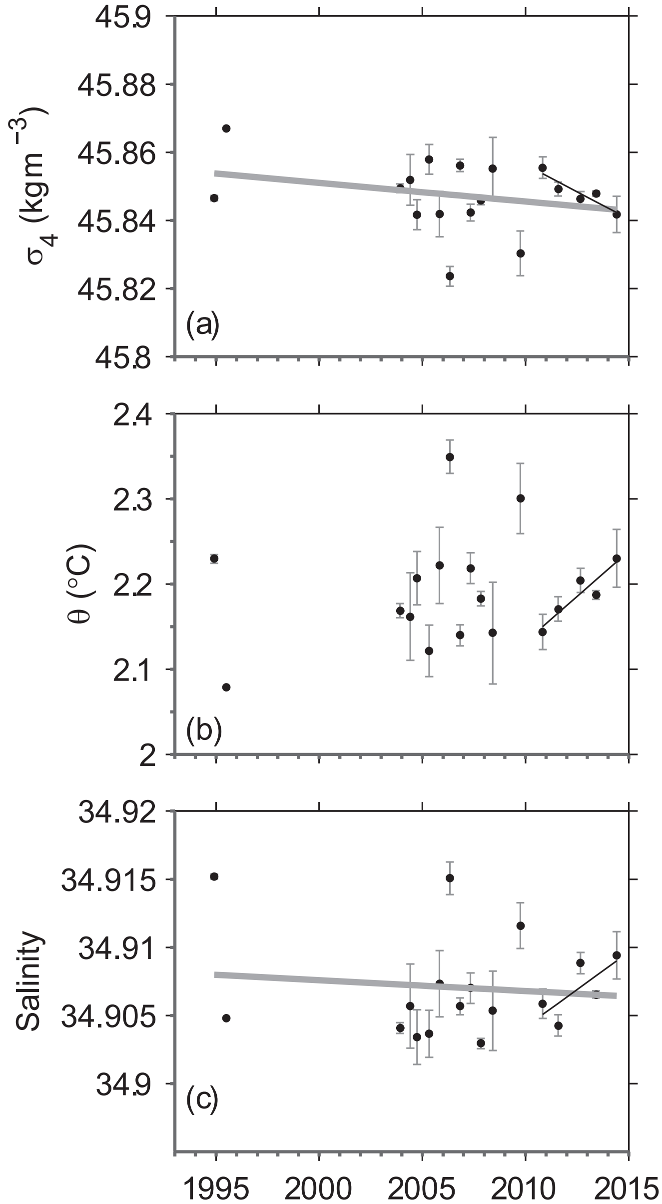

Fig. 10. Time series of DSOW properties at Line W averaged in the core where the CFC-11 concentration is $\geq 90\%$ of the deep maximum concentration showing (a) potential density, σ_4, (b) potential temperature referenced to 0 dbar, θ, and (c) salinity. In each panel, the error bars represent the standard deviation of the properties within the patch of DSOW used to calculate the averages (and in some cases the error bar spread is smaller than the symbol, e.g. 1994 and 1995). The 20-year linear trends (thick gray lines) are significantly different from zero at the 90% confidence level for σ_4 (-5.4×10^{-4} kg m^{-3} yr^{-1}) and salinity (-7.9×10^{-5} psu yr^{-1}) and not significantly different from zero for θ. If the data from the 1990s are excluded, none of the trends is significant. If only the most recent 5 years are considered (2010–2014), all three DSOW properties exhibit trends which are significantly different from zero at the 99% confidence level (thin black lines). Over this period σ_4 decreased at 3.2×10^{-3} kg m^3 yr^{-1}, θ increased at 2.1×10^{-2} °C yr^{-1} and salinity increased at 1.1×10^{-3} psu yr^{-1}.

These reported property ranges translate to $27.82<\sigma_0<27.97$ kg m^{-3} and $45.75<\sigma_4<46.06$ kg m^{-3}; the density of the DSOW core observed at Line W core also falls within this range (Fig. 10a). However, the lightest DSOW observed at Line W is slightly outside the range reported by Huhn et al. (2008) and used by Rhein et al. (2015): $45.83<\sigma_4<45.9$ kg m^{-3}.

For comparison with DSOW and to evaluate the evolution of the interior ocean seaward of the Gulf Stream, the interior's

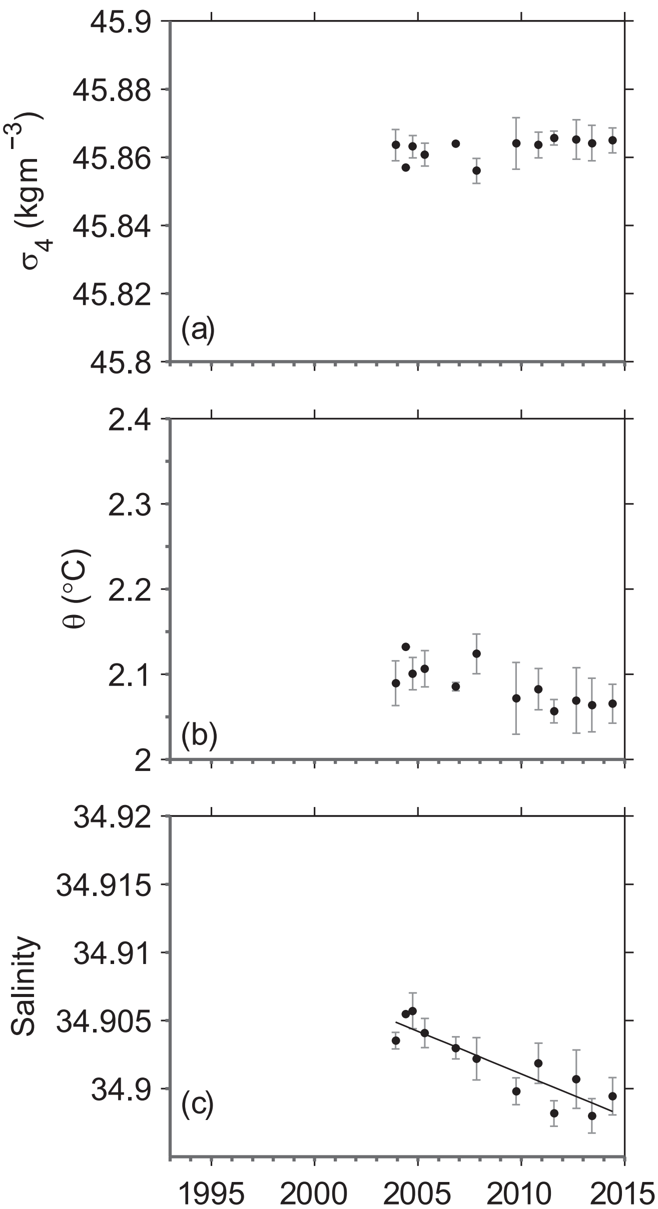

Fig. 11. Time series of properties of the deep interior at Line W showing (a) σ_4, (b) θ, and (c) salinity. These represent the properties averaged in the area denoted by the gray box in Fig. 8 for each of the 12 Line W sections that cross into the Sargasso Sea. Error bars represent the standard deviation of the properties within the area used to calculate the averages (note that some sections have no data at some interior stations) and in some cases the error bar spread is smaller than the symbol. The trend (black line) in (c) is significant at the 99% confidence level with salinity decreasing at 6.2×10^{-4} psu yr^{-1}.

properties are separately averaged for the 12 sections that extend into the Sargasso Sea at least to Station 20 (Fig. 11). In this case, the averaging is done for all gridded profiles that fall within the fixed area below 3000 dbar and between Stations 20 and 26 (demarcated by the gray box in Fig. 8).

The DSOW's and interior's evolutions are described further in sections 4.2.2 and 4.2.3. For all linear trends that are reported here, the significance level is established using a Student's t test with each section treated as an independent sample. With the time series of regular Line W sections just reaching a decade in length, however, separating linear trends from decadal (or longer period) variability is ambiguous.

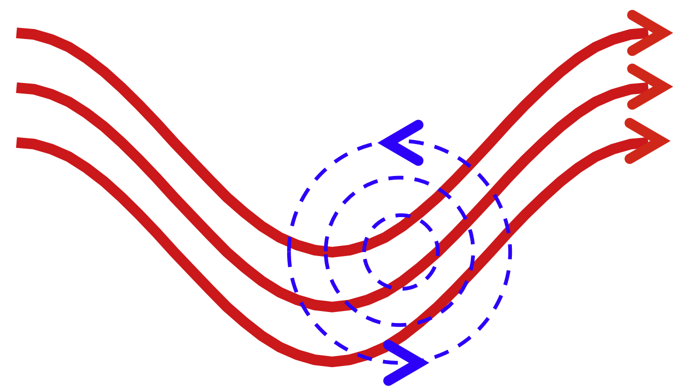

Fig. 12. Schematic representation of the upper layer (red) and lower layer (blue) velocities associated with deep cyclogenesis under a Gulf Stream meander trough. (For interpretation of the references to color in this figure legend, the reader is referred to the web version of this article.)

4. Impact of deep cyclogenesis on the evolution of DSOW

4.1. Gulf stream meanders, cyclogenesis, and the DSOW core

Previous studies have shown that the Gulf Stream path sometimes forms a quasi-stationary meander trough in the region where it crosses Line W (e.g., Shay et al., 1995; Watts et al., 1995). Based on a 2-year study from moorings in the Synoptic Ocean Prediction (SYNOP) Experiment's Central Array, Savidge and Bane (1999a) estimated that such a trough occurs about 35% of the time near 68 °W (the Central Array location is indicated by the green circle in Fig. 1). While these quasi-stationary path distortions cannot be discerned from the ensemble of Gulf Stream mean paths calculated from altimetry maps (Fig. 1, yellow contour), the finding of Savidge and Bane (1999a) is consistent with a partitioning of the LADCP sections and concurrent SSH snapshots (e.g., Fig. 2): a meander trough is present at Line W during 5 of the 18 sections (28% of the sections).

Deep cyclogenesis associated with Gulf Stream troughs has been studied based on the SYNOP observations (Savidge and Bane, 1999a), theoretical considerations (Savidge and Bane, 1999b) and a two-layer shallow-water model with a free surface (Kämpf, 2005). In these studies, a deep cyclone spins up beneath the Gulf Stream such that the cyclone's low-pressure center is offset from the Gulf Stream trough towards a downstream crest (Fig. 12). The trough and the associated deep cyclone develop in tandem through a barotropic–baroclinic instability mechanism (Kämpf, 2005) in which advection of relative vorticity in the upper layer is coupled to the deep layer which undergoes vortex tube stretching.

There are striking similarities between the deep cyclones described by these SYNOP studies and the circulation inferred here from the composited SSH maps and LADCP velocity sections for those Line W transects that cross a Gulf Stream trough (Fig. 6a). The LADCP and altimetry data indicate that when a large meander trough is present at Line W (i.e., when the Gulf Stream axis shifts offshore here), it is accompanied by deep cyclonic flow offset seaward from a closed SSH contour. This is suggested by the horizontal velocity vectors (averaged for the 5 sections sampling a trough) on the σ_4=45.86 kg m^{-3} isopycnal (Fig. 6a, blue arrows). Here the flow at Stations 16–18 is strong and towards the southwest. The vectors indicate weak flow at the center of the cyclone (Station 20) and a northeastward recirculation at Stations 21–23. The velocity vectors on this isopycnal indicate swirl speeds reaching 30 cm s^{-1} and a cyclone radius (distance to maximum velocity, taken here as ½ the distance between Stations 17 and 21) of about 75 km. These values for the composite cyclone (obtained by averaging data from 5 sections) are comparable to those reported for individual cyclones measured in SYNOP, where swirl speeds reached 50 cm s^{-1} and cyclone radius was typically 55 km (Savidge and Bane, 1999a). The slightly smaller, faster character of the individual SYNOP cyclones relative to the 5-cyclone composite is a consequence of averaging the features in physical space (rather than relative to each cyclone's center); this tends to weaken gradients so features have smaller amplitude and cover a larger area.

The Line W LADCP sections give no information on the persistence of each cyclone, but the upper ocean meander troughs (Shay et al., 1995) and the associated deep cyclones (Savidge and Bane, 1999a) observed in SYNOP typically lasted about 6–9 weeks. The troughs tended to intensify within the SYNOP array (i.e., near Line W) and then either decayed locally or moved towards the east out of the array.

In contrast to this deep cyclonic flow structure that accompanies a Gulf Stream trough, when there is no Gulf Stream meander in the upper layers (as indicated by SSH maps), the subsurface velocity structure does not show evidence of such a strong, large, deep cyclone (Fig. 6b, blue arrows).

Presumably, if a Gulf Stream trough at Line W eventually pinches off, the upper-ocean cyclonic circulation associated with the closed SSH contours (Fig. 6a, black contour) will become the center of a cold core ring isolated from the Slope Water (Iselin 1936; Stommel 1965) and confined to the Sargasso Sea side of the current. Unfortunately, since none of the LADCP sections examined here sampled through a cold core ring, these data cannot help resolve the deep structure of a pinched-off ring.

Interestingly, there seems to be a relation between the Gulf Stream path at Line W and the position of the DSOW's CFC concentration maximum identified with the tracers (Section 3.3). In the 18 sections examined here, the CFC concentration maximum is always located between 80 km and 200 km offshore of the shelf break (i.e., between Stations 9 and 13 over the 2600-m to 3800-m isobaths, Fig. 9a). The DSOW core is only located at Station 13 for three of the eighteen sections. Notably, each of these three most offshore-shifted DSOW occurrences and two of the occurrences of the DSOW CFC maxima at Station 12 coincide with the presence of a Gulf Stream trough on Line W. This supports the hypothesis that the deep cyclogenesis associated with Gulf Stream troughs draws the DSOW core offshore (as indicated in Fig. 8e) by advecting the DSOW core and sweeping it around the cyclone perimeter. For a 75-km radius cyclone and 30-cm s^{-1} swirl speed, persistence over 6 to 9 weeks allows a parcel to advect around the cyclone perimeter 2–3.5 times. Such stirring of the DSOW core into the interior is expected to enhance property gradients that drive isopycnal mixing between the DWBC and interior waters.

4.2. *Stirring DSOW into the deep interior by deep cyclones*

CFC-11 concentrations on Line W along the σ_4=45.86 kg m^{-3} isopycnal provide evidence of (irreversible) mixing between the DSOW and the interior and suggest that the mixing is enhanced by stirring due to the cyclones, as discussed above. To first order, the CFC-11 concentrations along the σ_4=45.86 kg m^{-3} isopycnal in each section decrease with distance from the western boundary (Fig. 13a). Superimposed on this overall decrease with distance is (1) the general increase in CFC concentrations over time from one section to the next due to the changing atmospheric concentrations at the formation region (e.g., compare the darker yellow shading in Fig. 8b's deep interior to the lighter yellow in Fig. 8a) and (2) meso-scale variability within some of the individual sections.

The sections' overall decrease in CFC-11 concentration away from the western boundary can be modeled as one-dimensional mixing using the diffusion equation (also called the heat equation):

$$\frac{\vartheta\eta}{\vartheta t}=\kappa\frac{\vartheta^2\eta}{\vartheta^2 x} \tag{1}$$

where t is time, x is distance from the western boundary where the CFC concentration maximum is located, κ is the eddy diffusivity, and η is the CFC-11 concentration, which is a function of both distance and time, $\eta(x, t)$. A simple way to conceptualize isopycnal mixing of the DSOW component of the DWBC with the abyssal interior along Line W is to consider the DSOW core as a continual source of CFCs to an infinite interior. For 1-dimensional

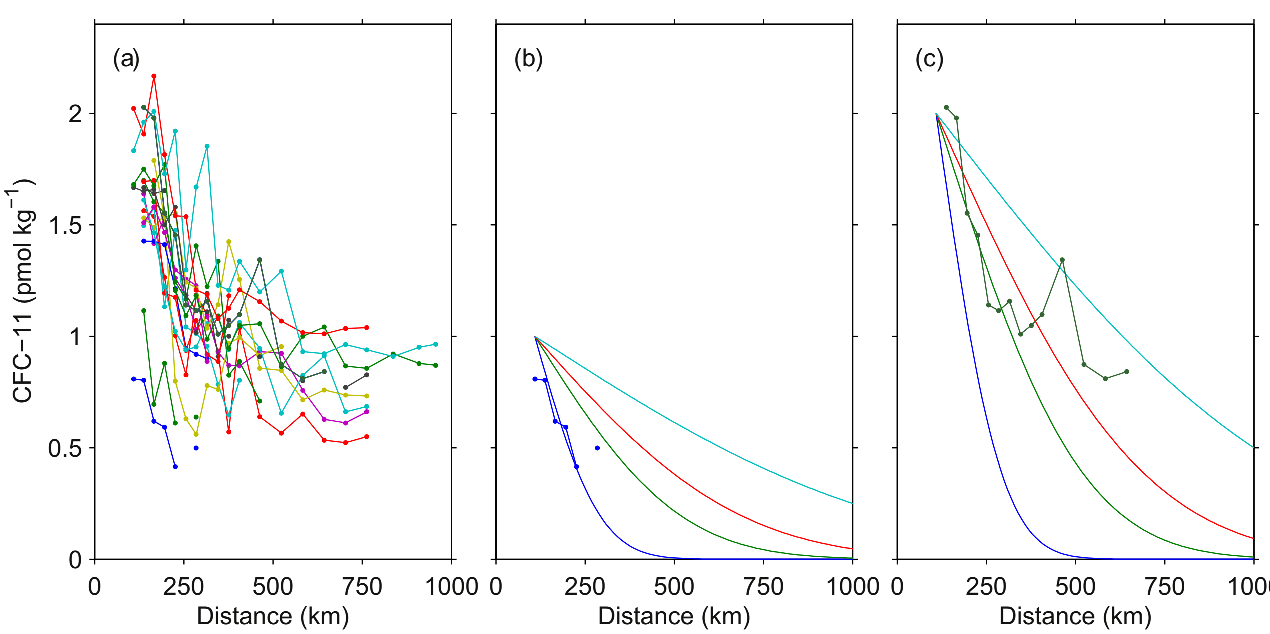

Fig. 13. Panel (a): CFC-11 concentrations along the σ_4=45.86 kg m^{-3} surface for each section. Panel (b): CFC-11 concentrations predicted by a 1-dimensional mixing model with n_o=1 pmol kg^{-1} at the western boundary and κ=300 m^2 s^{-1} (Eq. (2)). Concentrations are shown at t=1 (blue), 5 (green), 10 (red), and 30 (teal) years. Observed concentrations from Section 1 (November 1994) are superimposed (blue dots). Panel (c) is as in (b), but for a constant tracer source of n_o=2 pmol kg^{-1} with observed concentrations from Section 15 (July 2011) superimposed (green dots). (For interpretation of the references to color in this figure legend, the reader is referred to the web version of this article.)

mixing and a constant source of tracer with concentration η_o, the initial and boundary conditions for the partial differential equation in Eq. (1) are $\eta(x,0)=0$ and $\eta(0,t)=\eta_o$. The solution to Eq. (1) with these conditions is:

$$n(x,\ t) = n_o\ erfc\ \frac{x}{2\sqrt{\kappa t}} \tag{2}$$

Here erfc is the complementary error function. The evolution of CFC-11 concentration given by Eq. (2) is shown for $\kappa=300\ \mathrm{m}^2\ \mathrm{s}^{-1}$ and two values for n_o (Fig. 13b and c) – one representative of the concentration in the DSOW core in the mid 1990s and the other suitable for more recent CFC-11 concentrations in the DSOW.

The match between this idealized model and the observed concentration gradient along an isopycnal is reasonable for an early Line W section (Fig. 13b). At this time, the assumption in Eq. (2) of no tracer in the interior at the beginning of the mixing (i.e., the initial condition $\eta(x,0)=0$) is a sound representation of the real ocean. In addition, the mixing between the interior and DSOW is fast relative to changes in the DSOW's evolving CFC concentration so the system can be modeled as one with a constant CFC source (i.e., the boundary condition, $\eta(0,t)=\eta_o$).

However, the match is poor for the later section (regardless of the combination of n_o and κ used), particularly away from the western boundary (Fig. 13c). This mismatch is not surprising and results from the cumulative effect on the interior of the changing CFC-11 concentration in the DSOW core. While the solution in Eq. (2) assumes a constant boundary condition, the CFC-11 concentrations in the DSOW core is in fact strongly time dependent (Fig. 9b, black dots).

With a time dependent boundary condition, the solution to Eq. (1) takes a different form and can be calculated from the convolution of an exponential kernel (Fig. 14a) with the tracer concentration at the boundary. Given the same initial condition of no tracer in the interior and the boundary condition of CFC-11 concentration varying with time according to a function, h, such that $\eta(0,t)=h(t)$, the solution to Eq. (1) at time T is:

$$n(x,\ T) = \int_0^T \frac{x}{\sqrt{4\pi(T-t)^3}}\ exp\left(-\frac{x^2}{4\kappa(T-t)}\right)h(t)dt. \tag{3}$$

The form of $h(t)$ can be estimated from the observed CFC-11 concentrations in the DSOW core (Fig. 9b, black dots). Assuming CFC-11 concentration in the DSOW core was zero until around 1960 (CFCs were used before this time, but there is presumably a lag in their appearance along the deep western boundary at Line W, see also Smethie, 1993 for early CFC concentrations in the DWBC and interior here), a good fit to the data is given by:

$$h(t) = 0 \text{ for } t\ < 0 \text{ and } h(t) = 7.5\times10^{-4}t^2 \text{ for } t\ \geq 0 \tag{4}$$

where the concentration, h, is in pmol kg^{-1} and t is the years since 1960 (Fig. 14b).

Convolving the exponential kernel (Fig. 14a) with $h(t)$ (Fig. 14b) gives the concentrations predicted by the 1-dimensional mixing model in Eq. (3) (Fig. 14c). For $\kappa=300\ \mathrm{m}^2\ \mathrm{s}^{-1}$, the overall fit between the model and the observations is good not only for the early section (1994, blue) but also for the more recent section (2011, green). Despite this improvement, there are still mismatches between the 1-dimensional model and the observations. These are due to meso-scale heterogeneities in CFC concentration along the sections' 45.86 kg m^{-3} σ_4-surface which cannot be described by a 1-dimensional process.

These meso-scale heterogeneities point to a mechanism responsible for the exchange between the DSOW and interior, namely, stirring due to the deep cyclones, shown schematically in Fig. 15. As discussed in Section 4.1, Gulf Stream troughs in the upper ocean are accompanied by deep cyclones. At the radius of

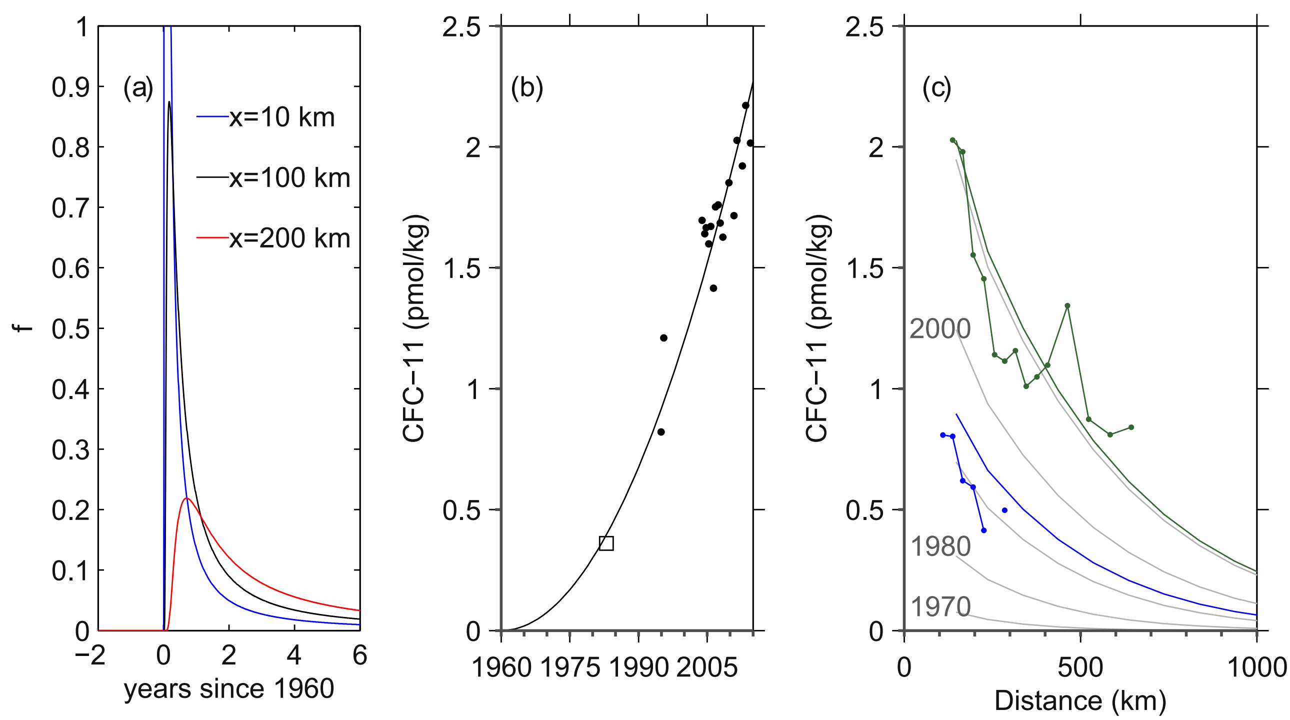

Fig. 14. Panel (a): the exponential kernel, f: $f=\frac{x}{\sqrt{4\pi t^3}}\ exp(-\frac{x^2}{4\kappa t})$, where x is the distance from the CFC-11 core and t is the years since 1960. Panel (b): fit to the observed CFC-11 concentrations in the DSOW core to determine $h(t)$ for Eq. (3). The dots are from the cruises listed in Table 2, the open square is from an earlier cruise in the region, OCE-134, which sampled the DSOW near Line W in 1983 (Smethie, 1993). The solid line shows the fit given by Eq. (4). Panel (c): CFC-11 concentrations predicted by Eq. (3) as a function of year and distance from the shelf break for 1970 through 2010 (gray curves) with 1994 (blue) and 2011 (green) highlighted and the corresponding observed CFC concentrations along Line W shown (blue and green dots). (For interpretation of the references to color in this figure legend, the reader is referred to the web version of this article.)

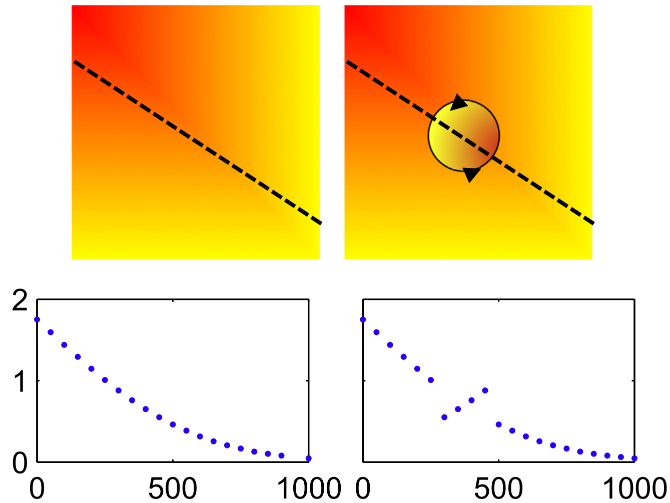

Fig. 15. Schematic representation of the effect of a deep cyclone on the background CFC concentration on an isopycnal surface. Left panels represent a plan view (top) and distance versus concentration (bottom) on an isopycnal surface on which the CFC gradient decreases monotonically away from the western boundary into the interior when there is no deep cyclone present. Right panels depict the effect of a deep cyclone on the concentration gradient: low concentrations (yellow shading) are advected onshore and high concentrations (red shading) are advected offshore by the cyclonic flow. Bottom panels show the concentrations along the dashed lines in the upper panels. (For interpretation of the references to color in this figure legend, the reader is referred to the web version of this article.)

maximum velocity (75 km), it was found that water parcels can be advected around the cyclone more than twice during the lifetime of a typical cyclone (Section 4.1); even at the DSOW core (~200 km from the cyclone center) the flow associated with the deep cyclone may draw the DSOW tracer core offshore, as indicated by the tendency for the DSOW core to appear around Station 12 or 13 rather than Station 10 or 11 when there is a large meander on the line (Section 4.1 and Fig. 9a). Furthermore, as waters swirl around in the deep cyclones, they may advect waters from regions with high CFC concentrations offshore – visible as localized concentration maxima in the interior (Fig. 13a). The section from July 2011, for example, exhibits such an interior concentration maximum at Station 21 about 460 km offshore of the shelfbreak (Fig. 13c). These regions of elevated concentration are left behind as the cyclone spins down and subsequently any associated local tracer maxima are eroded as the waters mix with the ambient waters.

4.3. Evolution of DSOW

4.3.1. The DSOW's CFC core and tracer ages

CFC concentrations and ratios in DSOW at Line W evolve over time due in part to changes in the source waters. Maximum CFC concentrations observed in DSOW at Line W have increased over time (Fig. 9b–d). CFC-11 and CFC-12 concentrations roughly doubled between 1994 and 2014 and CFC-13 increased almost 4-fold over the same 20-year period. Though the CFC concentrations in the DSOW at Line W should eventually decrease – due to the decreasing atmospheric concentrations of CFCs at the DSOW source (Fig. 3a) – this decrease in absolute concentrations is not yet evident at Line W, even in the most recent tracer measurements there. In light of the atmospheric CFC-11 and CFC-12 concentrations (Fig. 3a) – which have decreased since the 1990s and early 2000s, respectively – this suggests either very slow DSOW spreading along the western boundary (i.e. more than 10 years since formation) so that the DSOW with lower CFC 11 and CFC 12 concentrations has not yet reached Line W, or significant entrainment of older waters during DSOW overflow and spreading so

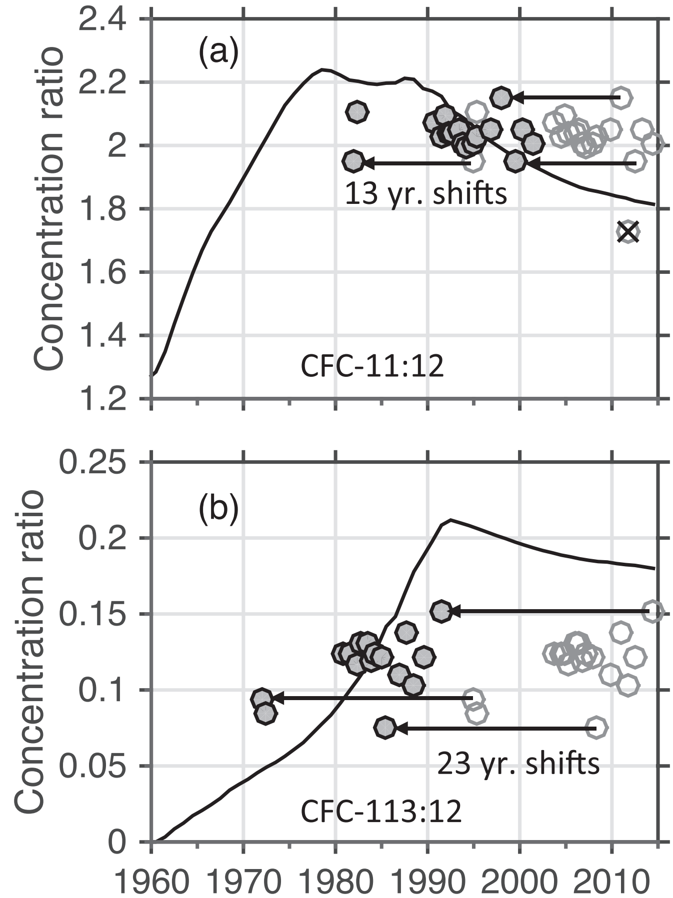

Fig. 16. Estimates of the ratio age of DSOW at Line W from (a) CFC-11:CFC-12 and (b) CFC-113:CFC-12. Each panel shows ratios expected for seawater in contact with the atmosphere (solid curves) for a water parcel at 1 °C and salinity of 34.9. This is within the range expected for the DSOW where it contacts the atmosphere (e.g., Tanhua, et al., 2005), though the curves' shapes change very little with temperature and salinity (see Fig. 3**c**). Note also that the ratios are independent of complete equilibration between seawater and atmosphere but do depend on equal saturations for the gases since unequal saturation can bias the ratio age at formation (e.g. Mecking et al., 2004). Panels also show: observed ratios from the DSOW CFC concentration maxima (open circles); and observed DSOW ratios shifted (filled circles) to optimize the fit to the solid curve (i.e., shifted by 13 years for CFC-11:CFC-12 in (a) and 23 years for CFC-113:CFC-12 in (b)). Open circle with the cross in panel (a) shows one point excluded from the CFC-11:CFC-12 ratio age calculation because the shift required to align it with the seawater curve (44 years) is more than three standard deviations from the mean shift.

that the CFC signature of younger waters is obscured by mixing with older waters. Both slow spreading and significant entrainment are consistent with Rhein et al. (2015) who report that the age of 'young' waters at Line W is about 20 years and that the fraction of 'young' waters here is about 0.5. Significant entrainment after the sill at Denmark Strait (e.g., Jochumsen et al., 2015) is also suggested by the increase in DSOW volume transport as it flows equatorward: the overflow is estimated at 3.4 Sv at the strait (Jochumsen et al., 2012) and 7.0 Sv for the DSOW layer at Line W (from the 4-year bias corrected mean of Toole et al., 2011). This entrainment may explain why the DSOW ratio ages at Line W (discussed below) are inconsistent with one another.

Unlike partial pressure CFC ages, which are functions of the percent equilibration between seawater and the atmosphere at the formation region, CFC ratio ages are independent of an assumed CFC % saturation for the gasses (e.g., Fine, 2011, and see also the caption to Fig. 16). DSOW ratio ages at Line W are obtained here by comparing the observed time series of CFC concentration ratios in DSOW with the time-history of CFC ratios expected for seawater that has been newly exposed to the atmosphere (Fig. 16a). The ratio age for DSOW estimated using the observed CFC-11:CFC-12 ratios at Line W (using the CFC maxima, representing the most unaltered DSOW, rather than the CFC concentrations averaged over the core) is 13 ± 5 years, while that estimated using the CFC-113:CFC-12 ratios is 23 ± 5 years (Fig. 16b). Each of these estimates is obtained by calculating the shift (in years) needed to align an observed CFC-11:CFC-12 (or CFC-113:CFC-12) ratio (open circles) onto the curve describing seawater in contact with the atmosphere (solid curve). The ranges reported here are the standard deviations of these shifts. For the CFC-11:CFC-12 ratio age calculation, one sample is excluded because its shift falls more than three standard deviations away from the mean (Fig. 16a, point denoted with the '*x*'). Also, because of the rise and subsequent fall of CFC-11:CFC-12 in seawater, there is ambiguity in whether the shifted data should be aligned to the ascending or the descending limb of the seawater curve. The descending limb is used here (giving 13 years), but shifting to the ascending limb gives a ratio age of 35 ± 6 years.

The discrepancy found here between ratio ages determined by the two different CFC ratios (13 ± 5 years versus 23 ± 5 years) suggests that there has been mixing between DSOW and ambient waters with non-zero CFC concentrations so that the ratios in the DSOW are *not* preserved. (Recall that for a ratio age to represent the true spreading rate from the source to a given location, there must either be no mixing or only mixing with an interior end-member that has essentially no dissolved CFCs.) Perhaps coincidentally, the CFC-113:CFC-12 ratio age calculated here is only slightly older than the age of 'young' DSOW at Line W reported by Rhein et al. (2015), which is about 20 years (based on their Fig. 2b) and which does not rest on the assumption of no mixing.

Indeed this ratio-age based evidence for mixing and exchange is consistent with the ever-increasing CFC concentrations in the interior along Line W (Fig. 9, gray dots) and suggests that CFC ratios are not only susceptible to alteration during DSOW formation and overflow processes but also during mixing with the interior all along the DWBC path (as also suggested for LSW by Bower et al., 2009), possibly via the deep cyclones as described in Section 4.2.

Despite the mismatch between the ratio ages (CFC11:CFC12 versus CFC113:CFC12), the spreading rates are calculated here for completeness and for comparison with LADCP measured velocities. Using the 13-year ratio age (from CFC11:CFC12) and 8000 km as the distance between Line W and the Denmark Strait suggests an equatorward spreading rate along the continental slope of about 2 cm s^{-1} for the DSOW core water properties, while the CFC-113:CFC-12 derived ratio age, 23 years, corresponds to a spreading rate of 1 cm s^{-1}. Both spreading rates inferred from the ratio ages are slower than the mean speeds indicated by the velocity sections (Figs. 4–6) and by the Line W moorings in which the mean speed in the DSOW core reaches 7 cm s^{-1} (Toole et al., 2011, Fig. 3). This mismatch is consistent with previous studies (e.g. Rhein, 1994). This is one manifestation of the misalignments between the DSOW tracer cores and velocity cores. Further, the time mean velocity structure observed at Line W (Toole et al., 2011 and this paper) may not be representative of the DWBC's velocity structure spatially averaged along its route between Denmark Strait and Line W (see also mean velocity sections in Fischer et al., 2015).

4.3.2. *Variability in DSOW properties*

Water properties of DSOW at Line W vary from one section to the next (Fig. 10). Year-to-year variations in the DSOW's θ_0 and salinity at Line W are strongly positively correlated (Fig. 17a) and to first order, this manifests as density compensation in the DSOW. However, the DSOW does exhibit a weak freshening trend over the 20-year period with salinity decreasing by 7.9×10^{-5} yr^{-1} (significant only at the 90% level). This freshening, coupled with no statistically significant trend in θ_0 to compensate over the long-term, leads to a slight decrease in the DSOW density over the 20-year period; σ_4 is decreasing at a rate of 5.4×10^{-4} kg m^{-3} yr^{-1} (significant at the 90% level). If the data from the 1990s are excluded, however, none of these trend estimates is significant since interannual variability dominates the records. East of Greenland, the DSOW core – identified with the θ_0 minimum rather than with CFCs – also exhibits no significant θ_0 or salinity trend between 1991 and 2011 (van Aken and de Jong, 2012).

In contrast to the weak (or non-existent) trends in DSOW properties over the long term (20 years), over the most recent 5 years (2010-2014), DSOW properties exhibit trends which are significant at the 99% confidence level: σ_4 is decreasing markedly at 3.2×10^{-3} kg m^{-3} yr^{-1}, driven by a sharp temperature increase with θ_0 increasing at 2.1×10^{-2} °C yr^{-1}. This recent density decrease in DSOW is occurring despite a weak salinity *increase* (1.1×10^{-3} yr^{-1}) over the same period (the recent salinity increase is opposite the long-term, weak freshening noted above). The time series of DSOW properties east of Greenland (van Aken and de

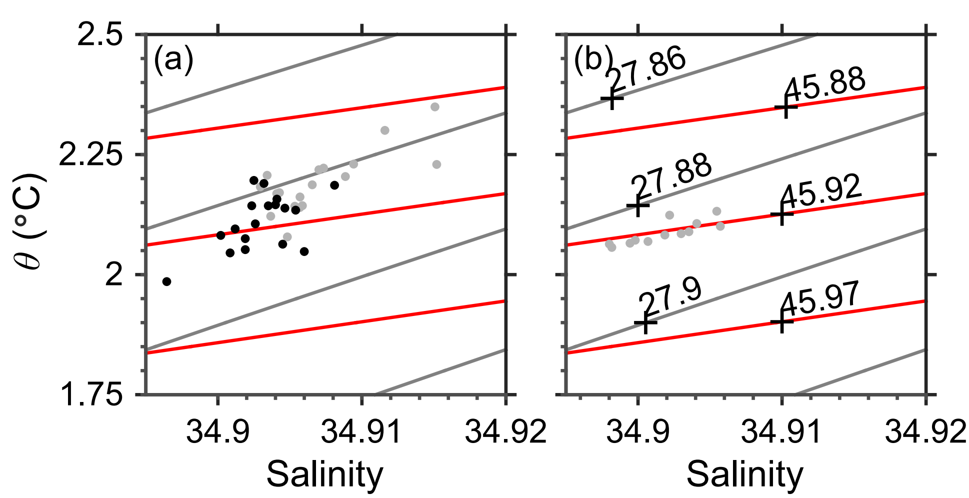

Fig. 17. Panel (a): relationship between salinity and θ (referenced to 0 dbar) in DSOW at Line W at the CFC maximum location (black dots) and averaged over the core of DSOW where CFC-11 concentration is $\geq 90\%$ of the concentration at the core (gray dots). Panel (b): as for (a) but in the deep interior averaged over the region indicated by the gray rectangle in Fig. 8. In both panels, the lines represent isopycnals for σ_0 (gray) and σ_4 (red). (For interpretation of the references to color in this figure legend, the reader is referred to the web version of this article.)

Jong, 2012, their Fig. 3) show the most pronounced period of sustained temperature increases in the record is accompanied by salinity increases. These commence in 2004 and continue to increase over four years in temperature and three years in salinity (with temperature increasing by ~0.5 °C and salinity by ~0.04). It is possible (though difficult to verify, since there is such strong inter and intra-annual variability in DSOW here, e.g. van Aken and de Jong, 2012; Jochumsen et al., 2015) that this signal east of Greenland is the precursor to the 2010–2014 increases observed at Line W. If so, this suggests (1) the advective timescale for property signals to propagate from southeastern Greenland to Line W is ~6 years; (2) the signals, which are only 10–15% as strong at Line W as they are east of Greenland, are likely diluted due to mixing with the interior along the DSOW's path; and (3) the recent increases observed in DSOW temperature and salinity at Line W are not likely indicative the beginning of a long-term trend.

4.4. Evolution of the deep interior

In the deep interior offshore of the Gulf Stream, water properties averaged between 400 km and 760 km (Stations 20 and 26) and between 3000 m and the seafloor indicate that the abyss here has been freshening at a rate of $6 \times 10^{-4}\,\mathrm{yr}^{-1}$ (significant at the 99% level, Fig. 11c) since at least 2003. (The earliest cruises at Line W in the 1990s did not reach into the Sargasso Sea.) This rate of freshening in the interior is an order of magnitude larger than the 20-year trend in the DSOW salinity and stands in stark contrast to the most recent (2010–2014) *increase* in DSOW salinity (Fig. 10c). The spatially-averaged temperature (θ) in the interior shows no significant trend (Fig. 11b). As in the DSOW, temperature and salinity are strongly positively correlated in the interior (Fig. 17b); due to this year-to-year density compensation – and despite the statistically significant trend in salinity – σ_4 does not exhibit a long-term trend in the interior (in contrast to σ_4 in the DSOW). This constant σ_4 in the interior is apparent in the θ–S plot in which the data cluster along the $\sigma_4 = 45.925\ \mathrm{kg\ m^{-3}}$ curve (Fig. 17b).

In addition to this abyssal freshening, the interior CFC concentrations have been slowly increasing since 2003, presumably as interior pathways and mixing between the DWBC and interior ocean have been delivering newly ventilated waters with ever increasing CFC concentrations (Fig. 9). As with the DSOW core (Section 4.2), it is expected that this increase in interior CFC concentrations will cease once the source waters that reach the interior are young enough to reflect the decreasing atmospheric concentrations of these tracers. Alternatively, this increase in interior CFC concentrations will cease when they are sufficiently diluted with older, CFC-free waters.

5. Summary and discussion

Shipboard observations collected over 20 years along Line W suggest exchange between the DSOW component of the DWBC and the interior here. Since the exchange mechanism inferred from the Line W observations may also occur elsewhere along the DWBC's route, significant exchange likely occurs not only during the DSOW overflow process, but also along the DSOW's transit towards the equator. At Line W, the CFC concentrations in the deep interior at the density level of the DSOW have been steadily increasing due to continued input of younger waters. This input is likely not just due to a peeling away of DWBC waters into the interior, but also includes alteration of the DWBC's DSOW tracer and velocity cores through entrainment of interior waters into the DWBC. This exchange is also implied by the mismatch in the DSOW's CFC-11:CFC-12 and CFC-113:CFC-12 ratio ages (13 versus 23 years), indicating mixing into the DSOW tracer core of older (interior) waters containing CFCs.

The time series built up by the Line W transects show that the deep interior's density has remained fairly steady since 2003 – despite a $6 \times 10^{-4}\,\mathrm{yr}^{-1}$ freshening – due to temperature compensation. In the DWBC, most of the long-term trends calculated for the DSOW are not significantly different from zero (or are only significant if the earliest transects from the mid-1990s are included in the analysis). During the most recent 5-year period (2010–2014), however, DSOW (identified by the CFC concentration core) has become lighter due to a steady warming (increasing by almost 0.1 °C) that is not compensated by the slight salinification (increasing by 0.003 psu).

Deep cyclogenesis under Gulf Stream troughs is a process that had been studied previously. However, the implication of these deep cyclones for stirring and mixing between the DWBC and interior was not fully appreciated. Evidence for cyclone-driven exchange comes from the combination here of satellite altimetry measurements with observations from the repeated shipboard velocity, tracer and water property transects. Concurrent LADCP and tracer data suggest that the circulation associated with ubiquitous cyclones may be a significant mechanism by which water is exchanged between the DWBC and the interior. Understanding this upper-ocean/deep-ocean coupling will likely help with the interpretation of transport variability observed with the 10-year DWBC Line W mooring array.

Since the Gulf Stream meanders vigorously beyond its separation from the western boundary near Cape Hatteras, particularly east of 70 °W (e.g., Fig. 1 and also Fig. 11 in Kelly et al., 2010), this deep cyclone-driven exchange may be important at multiple locations along the DWBC between Cape Hatteras and the Tail of the Grand Banks. This mechanism raises the possibility that the processes parameterized by the diffusion coefficient, κ, are location and time dependent, particularly if some years have a more unstable Gulf Stream (more meandering) than other years (as is the case, for example, in the Kuroshio Extension region, Qiu and Chen, 2005). This remains to be investigated further by examining interannual variability in Gulf Stream state (e.g., path length, position, strength, number and size of meanders) between Cape Hatteras and the Tail of the Grand Banks (as has been investigated for the Kuroshio Extension, Qiu and Chen, 2010). Additionally, further investigation of the coupling between the upper- and deep-ocean seems necessary.

Acknowledgments

The Line W program has been supported since 2004 by the US National Science Foundation with funding for the research here provided under grants OCE-0726720, 1332667 and 1332834. We gratefully acknowledge the careful comments of six reviewers.

References

Abraham, J.P., et al., 2013. A review of global ocean temperature observations: implications for ocean heat content estimates and climate change. Rev. Geophys. 51, 450–483. http://dx.doi.org/10.1002/rog.20022.

Bower, A.S., Hunt, H.D., 2000. Lagrangian observations of the Deep Western Boundary Current in the North Atlantic Ocean. Part I: Large-scale pathways and spreading rates. J. Phys. Oceanogr. 30 (5), 764–783.

Bower, A.S., Lozier, M.S., Gary, S.F., Böning, C., 2009. Interior pathways of the Atlantic Meridional overturning circulation. Nature 459 (14), 243–248. http://dx.doi.org/10.1038/ nature07979.

Bower, A.S., Hendry, R.M., Amrhein, D.E., Lilly, J.M., 2013. Direct observations of formation and propagation of subpolar eddies into the Subtropical North Atlantic. Deep-Sea Res. II 85, 15–41. http://dx.doi.org/10.1016/j.dsr2.2012.07.029.

Bullister, J.L., 2015. Atmospheric Histories (1765-2015) for CFC-11, CFC-12, CFC-113, CCl4, SF6 and N2O. NDP-095(2015). Carbon Dioxide Information Analysis Center, Oak Ridge National Laboratory, US Department of Energy, Oak Ridge,

Tennesseehttp://dx.doi.org/10.3334/CDIAC/otg.CFC_ATM_Hist_2015 ⟨⟨http://cdiac.ornl.gov/ftp/oceans/CFC_ATM_Hist/CFC_ATM_Hist_2015⟩⟩.
Cornillon, P., 1986. The effect of the New England Seamounts on Gulf Stream meandering as observed from satellite IR imagery. J. Phys. Ocean. 16, 386–389.
Egbert, G.D., Bennett, A.F., Foreman, M.G.G., 1994. TOPEX/Poseidon tides estimated using a global inverse model. J. Geophys. Res. 99, 24821–24852.
Egbert, G.D., Erofeeva, S.Y., 2002. Efficient inverse modeling of barotropic ocean tides. J. Atmos. Ocean. Technol. 19, 183–204.
Fischer, J., Karstensen, J., Zantopp, R., Visbeck, M., Biastoch, A., Behrens, E., Böning, C.W., Quadfasel, D., Jochumsen, K., Valdimarsson, H., Jónsson, S., Bacon, S., Holliday, N.P., Dye, S., Rhein, M., Mertens, C., 2015. Intra-seasonal variability of the DWBC in the western subpolar North Atlantic. Prog. Ocean. 132, 233–249. http://dx.doi.org/10.1016/j.pocean.2014.04.002.
Fine, R.A., Rhein, M., Andrié, C., 2002. Using a CFC effective age to estimate propagation and storage of climate anomalies in the Deep Western North Atlantic Ocean. Geophys. Res. Lett. 29 (24), 2227. http://dx.doi.org/10.1029/2002GL015618.
Fine, R.A., 2011. Observations of CFCs and SF_6 as ocean tracers. Annu. Rev. Mar. Sci. 3, 173–195. http://dx.doi.org/10.1146/annurev.marine.010908.163933.
Gawarkiewicz, G.G., Bahr, F., Beardsley, R.C., Brink, K.H., 2001. Interaction of a slope eddy with the shelfbreak front in the Middle Atlantic Bight. J. Phys. Ocean. 31, 2783–2796.
Hogg, N.G., 2000. Low-frequency variability on the western flanks of the Grand Banks. J. Mar. Res. 58, 523–545.
Huhn, O., Roether, W., Steinfeldt, R., 2008. Age spectra in North Atlantic Deep Water along the South American continental slope, 10N-30S, based on tracer observations. Deep-Sea Res. I 55 (10), 1252–1276.
Iselin, C.O.'D., 1936. A Study of the Circulation of the Western North Atlantic. Papers in Physical Oceanography and Meteorology 4. MIT and Woods Hole Oceanographic Institution, United States, p. 10.
Jochumsen, K., Quadfasel, D., Valdimarsson, H., Jónsson, S., 2012. Variability of the Denmark Strait overflow: Moored time series from 1996–2011. J. Geophys. Res. 117, C12003. http://dx.doi.org/10.1029/2012JC008244.
Jochumsen, K., Köllner, M., Quadfasel, D., Dye, S., Rudels, B., Valdimarsson, H., 2015. On the origin and propagation of Denmark Strait overflow water anomalies in the Irminger Basin. J. Geophys. Res. Ocean. 120, 1841–1855. http://dx.doi.org/10.1002/2014JC010397.
Johns, W.E., Shay, T.J., Bane, J.M., Watts, D.R., 1995. Gulf Stream structure, transport, and recirculation near 68°W. J. Geophys. Res. 100 (C1), 817–838. http://dx.doi.org/10.1029/94JC02497.
Joyce, T.M., Dunworth-Baker, J., Pickart, R.S., Torres, D., Waterman, S., 2005. On the deep western boundary current south of Cape Cod. Deep-Sea Res. II 52, 615–625.
Kämpf, J., 2005. Cyclogenesis in the deep ocean beneath Western Boundary Currents: a process-oriented numerical study. J. Geophys. Res. 110, C03001. http://dx.doi.org/10.1029/2003JC002206.
Kelly, K.A., Small, R.J., Samelson, R.M., Qiu, B., Joyce, T.M., Kwon, Y.-O., Cronin, M.F., 2010. Western boundary currents and frontal air–sea interaction: Gulf Stream and Kuroshio Extension. J. Clim. 23, 5644–5667. http://dx.doi.org/10.1175/2010JCLI3346.1.
LeBel, D.A., Smethie Jr., W.M., Rhein, M., Kieke, D., Fine, R.A., Bullister, J.L., Min, D.-H., Roether, W., Weiss, R.F., Andrie, C., Smythe-Wright, D., Jones, P., 2008. The formation rate of North Atlantic Deep Water and Eighteen Degree Water calculated from CFC-11 inventories observed during WOCE. Deep-Sea Res. I 55, 891–910. http://dx.doi.org/10.1016/j.dsr.2008.03.009.
McCartney, M.S., 1992. Recirculating components to the deep boundary current of the Northern North Atlantic. Progr. Ocean. 29, 283–383.
Mecking, S., Warner, M.J., Greene, C.E., Hautala, S.L., Sonnerup, R.E., 2004. The effects of mixing on CFC concentrations and CFC-derived age distributions in the North Pacific thermocline. J. Geophys. Res. 109, C07014. http://dx.doi.org/10.1029/2003JC001988.
Meinen, C.S., Johns, W.E., Garzoli, S.L., van Sebille, E., Rayner, D., Kanzow, T., Baringer, M.O., 2013. Variability of the Deep Western Boundary Current at 26.51°N during 2004–2009. Deep-Sea Res. II 85, 154–168. http://dx.doi.org/10.1016/j.dsr2.2012.07.036.
Millard, R.C., Yang, K., 1993. CTD Calibration and Processing Methods used at Woods Hole Oceanographic Institute. WHOI Technical Report, United States, p. 96.
Peña-Molino, B., Joyce, T.M., Toole, J.M., 2011. Recent changes in the Labrador Sea Water within the Deep Western Boundary Current southeast of Cape Cod. Deep-Sea Res. I 58, 1019–1030.
Pickart, R.S., 1995. Gulf Stream-generated topographic Rossby waves. J. Phys. Ocean. 25, 574–586.
Pickart, R.S., 1994. Interaction of the Gulf Stream and the Deep Western Boundary Current where they cross. J. Geophys. Res. 99, 25155–25164.
Pickart, R.S., Smethie Jr., W.M., 1993. How does the Deep Western Boundary Current cross the Gulf Stream? J. Phys. Ocean. 23, 2602–2616.
Pickart, R.S., Smethie Jr., W.M., 1998. Temporal evolution of the deep western boundary current where it enters the sub-tropical domain. Deep. Sea Res. 45, 1053–1083.
Pickart, R.S., Hogg, N.G., Smethie Jr., W.M., 1989. Determining the strength of the deep western boundary current using the chlorofluoromethane ratio. J. Phys. Ocean. 19, 940–951.
Pickart, R.S., Spall, M.A., Lazier, J.R.N., 1997. Mid-depth ventilation in the western boundary current system of the sub-polar gyre. Deep-Sea Res. I 44, 1025–1054.
Prinn, R.G., Weiss, R.F., Fraser, P.J., Simmonds, P.G., Cunnold, D.M., 2000. A history of chemically and radiatively important gases in air deduced from ALE/GAUGE/AGAGE. J. Geophys. Res. 105, 17751–17792.
Qiu, B., Chen, S., 2005. Variability of the Kuroshio Extension jet, recirculation gyre and mesoscale eddies on decadal timescales. J. Phys. Ocean. 35, 2090–2103.
Qiu, B., Chen, S., 2010. Eddy-mean flow interaction in the decadally modulating Kuroshio Extension system. Deep.-Sea Res. II 57, 1098–1110. http://dx.doi.org/10.1016/j.dsr2.2008.11.036.
Rhein, M., 1994. The deep western boundary current: tracers and velocities. Deep-Sea Res., Part 1 41 (2), 263–281.
Rhein, M., Kieke, D., Steinfeldt, R., 2015. Advection of North Atlantic Deep Water from the Labrador Sea to the southern hemisphere. J. Geophys. Res. Ocean. 120, 2471–2487. http://dx.doi.org/10.1002/2014JC010605.
Richardson, P., 1985. Average velocity and transport of the Gulf Stream near 55 W. J. Mar. Res. 43 (1), 83–111. http://dx.doi.org/10.1357/002224085788437343.
Rossby, T., Flagg, C.N., Donohue, K., Sanchez-Franks, A., Lillibridge, J., 2014. On the long-term stability of Gulf Stream transport based on 20 years of direct measurements. Geophys. Res. Lett. 41, 114–120. http://dx.doi.org/10.1002/2013GL058636.
Savidge, D.K., Bane Jr., J.M., 1999a. Cyclogenisis in the deep ocean beneath the Gulf Stream 1. Description. J. Geophys. Res. 104 (C8), 18,111–18,126.
Savidge, D.K., Bane Jr., J.M., 1999b. Cyclogenisis in the deep ocean beneath the Gulf Stream 2. Dynamics. J. Geophys. Res. 104 (C8), 18,127–18,140.
Schott, F.A., Brandt, P., 2007. Circulation and Deep Water Export of the Subpolar North Atlantic During the 1990's. In: Schmittner, A., Chiang, J.C.H., Hemming, S. R. (Eds.), Ocean Circulation: Mechanisms and Impacts-Past and Future Changes of Meridional Overturning. American Geophysical Union, Washington, D.Chttp://dx.doi.org/10.1029/173GM08.
Shay, T.J., Bane, J.M., Watts, D.R., Tracey, K.L., 1995. Gulf Stream flow field and events near 68 W. J. Geophys. Res. 100 (C11), 22,565–22,589.
Smethie Jr., W.M., 1993. Tracking the thermohaline circulation in the western North Atlantic using chlorofluorocarbons. Prog. Ocean. 31, 51–99.
Smethie Jr., W.M., Fine, R.A., Putzka, A., Jones, E.P., 2000. Tracing the flow of North Atlantic deep water using chlorofluorocarbons. J. Geophys. Res. 105, 14297–14323.
Smethie, W.M., Jr., Smith, J.N., Curry, R.G., Transient Tracer Evidence for an Internal Flow Path of Denmark Strait Overflow Water from the Subpolar to the Subtropical Western North Atlantic Ocean, Abstract OS21A-1663 presented at 2012 Fall Meeting, AGU, San Francisco, Calif., 3-7 Dec.
Spall, M.A., 1996. Dynamics of the Gulf Stream/Deep Western Boundary Current Crossover. Part I: entrainment and recirculation. J. Phys. Ocean. 26 (10), 2152–2168.
Stommel, H.M., 1965. The Gulf Stream: A Physical and Dynamical Description, 2nd ed. University of California Press, Berkeley, and Cambridge University Press, London, p. 248.
Swift, J.H., 1994. The circulation of the Denmark Strait and Iceland-Scotland Overflow Waters in the North Atlantic. Deep. Sea Res. 31, 1339–1355.
Tanhua, T., Olsson, K.A., Jeansson, E., 2005. Formation of Denmark Strait overflow water and its hydro-chemical composition. J. Mar. Res. 57, 264–288. http://dx.doi.org/10.1016/j.jmarsys.2005.05.003.
Talley, L.D., McCartney, M.S., 1982. Distribution and circulation of Labrador Sea Water. J. Phys. Ocean. 12, 1189–1205.
Thompson, R.O.R.Y., Luyten, J.R., 1976. Evidence for bottom-trapped topographic Rossby waves from single moorings. Deep-Sea Res. 23, 629–635.
Toole, J.M., Curry, R.G., Joyce, T.M., McCartney, M., Pena-Molino, B., 2011. Transport of the North Atlantic Deep Western Boundary Current about 39N, 70W: 2004-2008. Deep. Sea -Res. II 58, 1768–1780. http://dx.doi.org/10.1016/j.dsr2.2010.10.058.
Thurnherr, A.M., 2010. A practical assessment of the errors associated with full-depth LADCP profiles obtained using Teledyne RDI Workhorse acoustic Doppler current profilers. J. Atmos. Ocean. Technol. 27, 1215–1227.
Våge, K., Pickart, R.S., Spall, M.A., Valdimarsson, H., Jónsson, S., Torres, D.J., Østerhus, S., Eldevik, T., 2011. Significant role of the North Icelandic Jet in the formation of Denmark Strait overflow water. Nat. Geosci. 4, 723–727. http://dx.doi.org/10.1038/NGEO1234.
van Aken, H.M., de Jong, M.F., 2012. Hydrographic variability of Denmark Strait Overflow Water near Cape Farewell with multi-decadal to weekly time scales. Deep-Sea Res. 66, 41–50. http://dx.doi.org/10.1016/j.dsr.2012.04.004.
Visbeck, M., 2002. Deep velocity profiling using lowered acoustic Doppler current profilers: bottom track and inverse solutions. J. Atmos. Ocean. Technol. 19, 794–807.
Walker, S.J., Weiss, R.F., Salameh, P.K., 2000. Reconstructed histories of the annual mean atmospheric mole fractions for the halocarbons CFC-11 CFC-12, CFC-113, and carbon tetrachloride. J. Geophys. Res. 105 (C6), 14,285–14,296. http://dx.doi.org/10.1029/1999JC900273.
Wallace, D.W.R., 1995. Anthropogenic chlorofluoromethanes and the seasonal mixing rates in the Middle Atlantic Bight. Deep. Sea Res. 41, 307–324.
Watts, D.R., 1991. Equatorward currents in temperatures 1.8–6.0 °C on the continental slope in the Mid-Atlantic Bight. In: Chu, P.C., Gascard, J.C. (Eds.), Deep Convection and Deep Water Formation in the Ocean, pp. 183–196.
Watts, D.R., Tracey, K.L., Bane, J.M., Shay, T.J., 1995. Gulf Stream path and thermocline structure near 74 W and 68 W. J. Geophys. Res. 100 (C9), 18,291–18,312.
Worthington, L.V., Wright, W.R., 1970. North Atlantic Ocean Atlas of Potential Temperature and Salinity in the Deep Water, Including Temperature, Salinity, and Oxygen Profiles From the Erika Dan cruise of 1962 2. Woods Hole Oceanographic Institution Atlas Series, United States.